THE UNIVERSITY OF MICHIGAN

COLLEGE OF ENGINEERING
Department of Electrical Engineering
Space Physics Research Laboratory

Scientific Report No. GS-2

AN EJECTABLE ION TRAP—LANGMUIR PROBE EXPERIMENT FOR IONOSPHERE DIRECT MEASUREMENTS

Prepared on behalf of the project by:

L. H. Brace M. Kanal J. R. Caldwell

ORA Project 03484

under contract with:

UNITED STATES AIR FORCE
GEOPHYSICS RESEARCH DIRECTORATE
ELECTRONIC SYSTEMS DIVISION
AIR FORCE SYSTEMS COMMAND
CONTRACT NO. AF 19(604)-6124
LAURENCE G. HANSCOM FIELD
BEDFORD, MASSACHUSETTS

administered through:

OFFICE OF RESEARCH ADMINISTRATION ANN ARBOR

July 1962

TABLE OF CONTENTS

Page

TABLE OF CONTENTS (Concluded)

LIST OF FIGURES

Figure Page

LIST OF FIGURES (Continued)

Figure Page

LIST OF FIGURES (Concluded)

LIST OF SYMBOLS

Cylindrical Probe Symbols

u_x, p	radial and tangential velocity components of a particle, respectively, at the sheath edge with respect to the moving probe;to be considered positive when directed toward the collector
C_m	most probable velocity of the particles = $\sqrt{2kT/m}$
W	drift velocity of the probe
λ	ratio of the drift velocity of the probe to the most probable velocity of the particles = W/C_m
θ	angle between the drift velocity vector W and axis of the cylinder
κ	$= \lambda \sin \theta$
T	temperature (°K)
N	number of particles per cubic meters
e	unit charge, 1.602×10^{-19} coulombs
m	mass of a particle in kgm
k	Boltzmann's constant, 1.3803×10^{-23} joule/°K
V	potential of the collector with respect to the plasma
$\mathcal{V}$	normalized potential = eV/kT
I	current to the collector
I_n	normalized current = $I/\sqrt{kT/2m\pi}\, Ne A_c$
A_c	area of the collector
a	radius of the sheath
r	radius of the collector
L	length of the collector
δV	voltage applied between the cylindrical collector and the 8-inch grid

LIST OF SYMBOLS (Continued)

8-Inch Ion Trap Probe Symbols

u_s, p_s	radial and tangential velocity components of a particle, respectively, at the sheath edge with respect to the moving probe
u_g, p_g	radial and tangential velocity components of a particle, respectively, at the grid surface
W	drift velocity of the probe
C_m	most probable velocity of the particles = $\sqrt{2kT/m}$
λ	ratio of the drift velocity of the probe to the most probable velocity of the particles = W/C_m
k	Boltzmann's constant, 1.3803×10^{-23} joule/°K
T	temperature (°K)
e	unit charge, 1.602×10^{-19} coulombs
m	mass of a particle in kgm
r_c	radius of the collector = 3.5 inches
r_g	radius of the grid = 4 inches
γ_o	a design constant = $\sqrt{r_c^2/(r_g^2-r_c^2)} = 1.8$
a	radius of the sheath
τ	$= \sqrt{a^2/(a^2-r_g^2)}$
d	diameter of each hole = 0.25 inches
t	thickness of the grid = 0.04 inches
ϕ	design angle defined as $\tan \phi = d/t = 6.25$
η	transparency coefficient of the grid; the ratio of the total hole area to the entire area of an 8-inch diameter sphere = 0.125
A_c	area of the collector
N	number density of the particles

LIST OF SYMBOLS (Concluded)

V_w	equilibrium potential of the grid with respect to the plasma
V_a	voltage applied between the collector and the grid
$\overline{V}_w$	normalized $V_w = eV_w/kT$
$\overline{V}_a$	normalized $V_a = eV_a/kT$
Λ	a function defined on page 34
H	a function defined on page 34.

ABSTRACT

This report reviews the history, theory and implementation of a rocket borne, ejectable ionosphere probe which combines a spherical ion trap and a thin cylindrical Langmuir probe developed by The University of Michigan scientists for use in their ionosphere research program. The theories of the Langmuir probe and the spherical ion trap are treated separately with emphasis upon the effect of the motion of the device relative to the plasma and, in the case of the Langmuir probe, its orientation with respect to the velocity vector. The theories are applied to predict the Langmuir probe and ion trap volt-ampere characteristics expected for typical F_1 region conditions. The interpretation of such characteristics in terms of ion and electron temperature and density is outlined. A detailed account of the design and engineering of the instrument is given. Plans for future use of the device are given in the Conclusion, where it is noted that the technique has the advantage of measuring the ion and electron temperatures simultaneously and thus is well suited to study of the question of thermal equilibrium as well as providing gas temperature profiles of the atmosphere.

1.0. INTRODUCTION

1.1. HISTORY

In the investigation of newly attainable regions of physical interest, it is natural to adopt measuring tools and techniques which have proved useful in earlier, similar studies. Thus, when V-2 rockets became available to scientists after World War II, several University of Michigan investigators suggested and directed the application of Langmuir probes, commonly used in gaseous conduction studies, to ionosphere research.[1-3] Each of three of these rockets carried, among many other experiments, an unsymmetrical bipolar probe. The collector geometry, dictated by practical considerations of space and compatibility with other experiments, was less than ideal; however, enough information was obtained to indicate that the technique, more carefully implemented, might prove to be a valuable tool in ionosphere research. Later, when smaller research rockets capable of reaching the ionosphere were developed, this laboratory, with the support of AFCRC, BRL, and later NASA,* renewed its ionosphere research effort. The rather unusual concept of an ejectable Langmuir probe, containing its own current detection and telemetry system, was implemented to insure that (a) the collector design need not be prejudiced by vehicle imposed limitations, and (b) the probe remain well away from local disturbances of the ionosphere due to outgassing from the burned out rocket motor as well as surface contaminants. Two different probe con-

---

*Air Force Cambridge Research Laboratories, Ballistic Research Laboratories and National Aeronautics and Space Administration.

figurations have been developed: the first, a Dumbbell-shaped bipolar probe used extensively and discussed elsewhere,[4-6] the second a combination spherical ion trap and Langmuir probe, which is the subject of this report.

Early ionosphere measurements by the Dumbbell probe technique revealed unexpectedly high daytime electron temperatures, which were interpreted as evidence against thermodynamic equilibrium since equally high gas temperature appeared unlikely.

It occurred to The University of Michigan investigators that this problem could be studied more directly by the simultaneous measurement of ion and electron temperature by means of a combined ion trap—Langmuir probe ejectable instrument. Since ion and gas temperature can differ little in the F region and below, the ion temperature measurements would be equivalent to an actual direct measurement of gas temperature, a much more difficult parameter to obtain. Thus, an existing unsymmetrical Langmuir probe instrument, consisting of a small cylindrical probe mounted on a 7-inch diameter sphere, was modified by enclosing it within an 8-inch perforated sphere, or grid, separated by suitable insulators. The pair of concentric spheres thus form an ion trap when the enclosed sphere is swept through a suitable range of voltages with respect to the outer grid which floats at its equilibrium potential in the plasma. The resulting current reaching the inner sphere is measured and telemetered to earth, where it is later interpreted in terms of ion and electron temperature and density.

The Langmuir probe portion of the experiment uses the 8-inch spherical grid as a plasma reference from which a thin cylindrical probe is swept through a suitable voltage range, and the resulting probe current is telemetered. These current characteristics provide a measurement of electron and ion density and electron temperature. The experiment is programmed to operate alternately in the ion trap and Langmuir probe modes throughout the flight. The two experiments are entirely independent and sufficiently redundant that a great deal of confidence can be had in the results, if self consistency exists. The instrument is shown fully assembled in Fig. 1a and, with half of the grid removed exposing the 7-inch inner sphere, in Fig. 1b.

In operation, the sphere is carried to the ionosphere in a specially designed nose cone, shown in Fig. 2, and is there ejected to carry out its measurement <u>undisturbed by the vehicle</u>.

The first 8-inch sphere launching was attempted in March, 1960 at Fort Churchill, Manitoba, in conjunction with a Dumbbell probe launching. The Dumbbell was launched successfully in the late afternoon aboard an Aerobee 300 which was to be followed by a sunset launching of the sphere on a Nike-Asp. Unfortunately, the Nike-Asp motor "broke-up" during the boost phase and the sphere nose cone was apparently struck and shattered by the Nike booster. The sphere came through the breakup in operating condition and continued to telemeter normal in-flight calibration curves until impact, some 60 sec after launch.

The cause of the breakup was not definitely established but it appeared that a poorly secured Nike launcher was at least a contributing factor, since at the instant of launch the launcher was lifted from its moorings and thrown against the opened roof of the Nike launcher building causing extensive damage.

Since that time, another 8-inch sphere package, essentially identical to the first, has been built. Unwilling to risk the payload on another Nike-Asp or to accept the low altitude of a Nike-Cajun, we permitted the sphere to lay idle while pursuing the more successful Dumbell probe technique.

When the 9-inch diameter Exos vehicle (using the Yardbird third stage) became available in 1961, renewed effort to launch the sphere was begun. Shortly, however, trouble developed in the Yardbird when used on other flights, and our launching was further delayed while this was being corrected. Subsequent static firings have shown that a nozzle redesign was required, and this problem has now apparently been resolved. Present plans call for the launching of the 8-inch sphere in the summer of 1962; and a second sphere, now under construction, is scheduled for the fall. Both will be launched at Eglin Air Force Base, Florida.

1.2. THE REGION OF MEASUREMENT

At all altitudes in the Earth's atmosphere a significant and measurable quantity of free charged particles exist. Below 70 or 80 km these normally exist primarily as positive and negative ions, while above 100 km, the charge takes the form of positive ions and electrons. Classical Langmuir probe theory is valid only where the mean free path of the ions is long compared to the Debye shielding distance (approximately the dimensions of the positive ion sheath of the collector); above 90 km for typical probes. Below this altitude, conductivity theory may be used to interpret the measured currents. The 8-inch sphere experiment, as it is called, was designed primarily for ionosphere measurements in the long mean-free-path region, thus the <u>lower</u> altitude

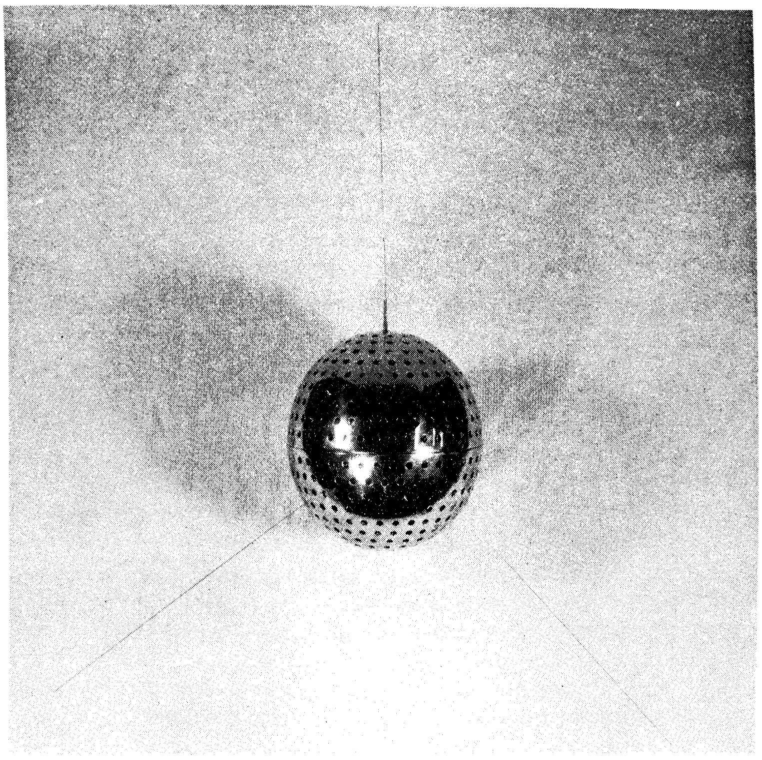

Fig. 1a. Photograph of the 8-inch sphere experiment, fully assembled.

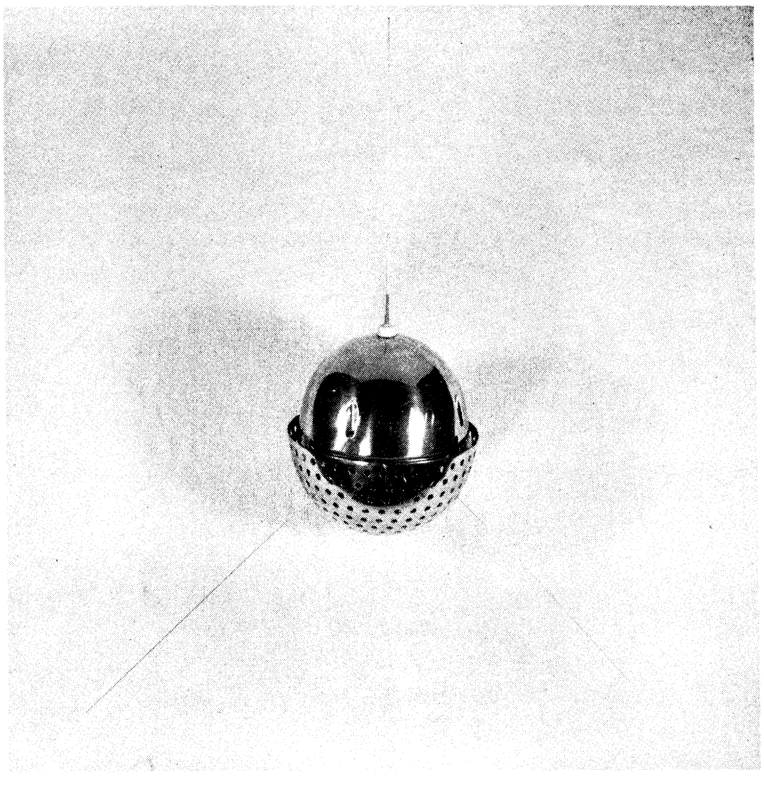

Fig. 1b. 8-inch sphere with half of the perforated sphere removed, showing the inner 7-inch diameter collector.

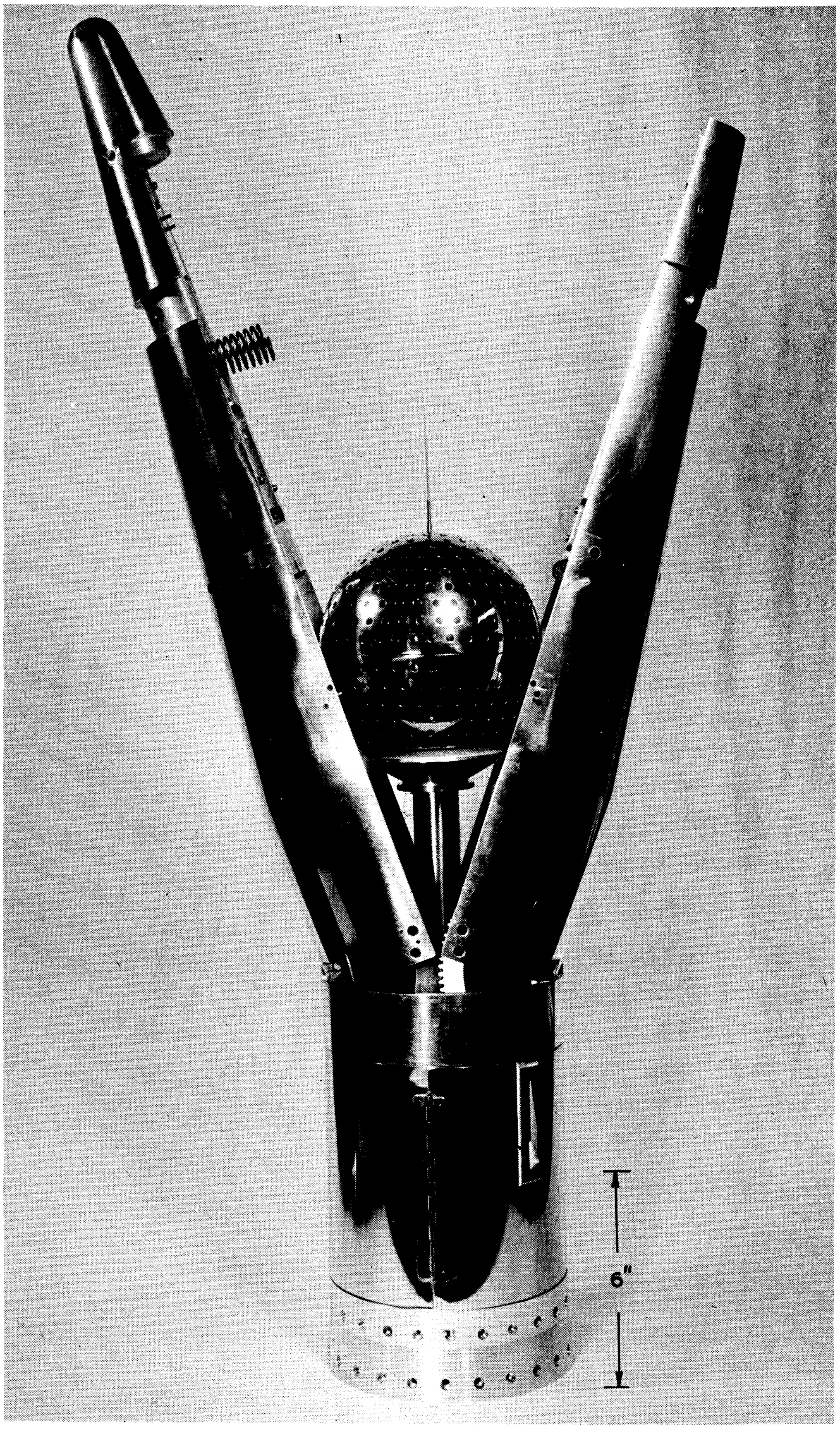

Fig. 2. Sphere in open nose cone.

limit of the experiment may be taken as approximately 90 km.

The upper altitude limit of the experiment is fixed by a number of variables, both ionospheric and instrumental. The theory assumes that a Maxwellian velocity distribution exists in the plasma, an assumption which has been questioned for the exosphere and is certainly suspect at altitudes where solar winds account for a significant portion of the random current density. However, satellite probe measurements to over 1,000 km show the distribution to be essentially Maxwellian.

A second factor in the upper altitude limit of the technique is the solar-induced photo-emission from the collector surfaces. This appears to become a significant positive current component above 1000 km in the daytime. As such, it must be considered in the reduction of ion density data, but does not seriously affect the measurement of electron temperature until much higher altitudes. Photo-emission is, of course, not a factor in a nighttime measurement.

A third and final factor, which primary affects the upper altitude limit of the Langmuir probe portion of the experiment, is the practical matter of the thickness of the ion sheath about the 8-inch perforated sphere. The cylindrical guard electrode is most effective when it extends beyond this sheath. The spherical sheath grows with decreasing ion density and approaches the guard length at a density of approximately 1×10^4 ions/cc, normally somewhat above 1000 km.

In summary, the region of the ionosphere for which this particular probe is applicable extends from approximately 90 to 1000 km in the daytime, and to somewhat higher altitudes at night. In the following section a review of the cylindrical probe and the ion trap theories is given, and several predicted volt-ampere characteristics of each are plotted and discussed. The more comprehensive theoretical treatments, from which the following sections are drawn, will be presented in report form in the near future.

2.0. THEORY OF THE EXPERIMENT

2.1. THE CYLINDRICAL LANGMUIR PROBE

2.1.1. Introduction.—Figure 3 is a simplified block diagram of the 8-inch sphere shown in its Langmuir probe mode of operation. In this mode, the perforated 8-inch sphere is shorted to the inner 7-inch sphere, and the pair act as a voltage reference in the plasma for the cylindrical probe. In operation a series of modified sawtooth waveforms (shown in the same figure) is impressed between the probe and the sphere. The resulting current characteristics are sensed by the current detector, I, telemetered to a ground station, and there recorded for future analysis in terms of the electron and ion density and electron temperature in the regions traversed by the probe.

The Langmuir probe sensor consists of a pair of spring-mounted concentric cylinders, insulated from each other and from the inner sphere on which the probe is mounted. The outer electrode, the guard, covers the inner electrode, the collector, for approximately 1/3 of the entire probe length and serves to (1) physically isolate the collector from the disturbing ion sheath which surrounds the sphere, and (2) electrically reduce the "fringe effects." Although the guard and collector are swept through the same range of potentials, only the collector current is measured. The cylindrical probe can be seen in Figs. 1, 2, 3, and 37.

Since, in rocket application, the probe package will reach velocities up to several times the most probable ion velocity, the classical Langmuir probe equation[7] for ion current no longer applies. The electron current func-

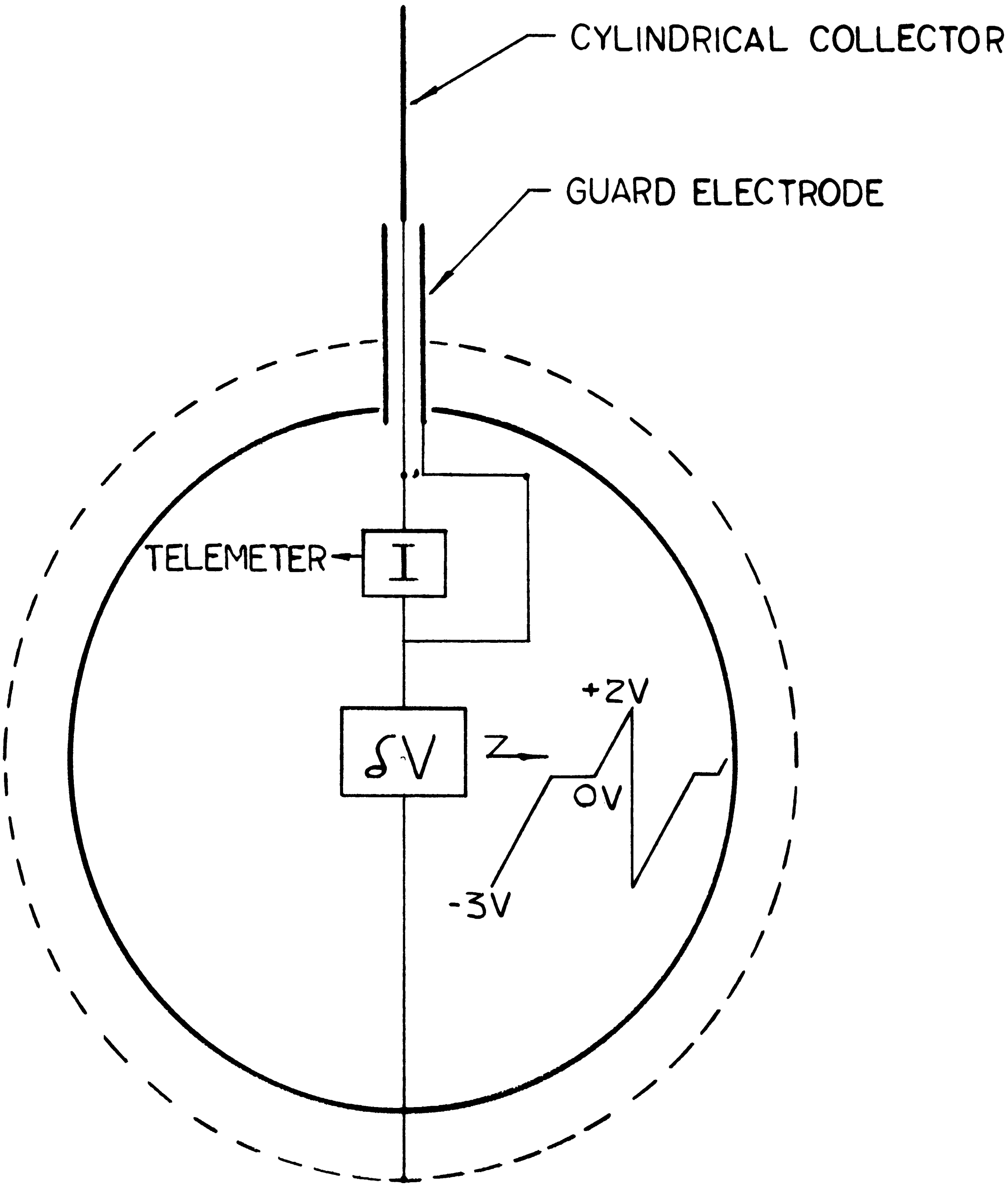

Fig. 3. Simplified block diagram of the 8-inch sphere shown in its Langmuir probe mode of operation.

tion is unchanged, however, since the average electron velocity in the ionosphere greatly exceeds expected rocket and even satellite velocity. To account for the effect of probe motion upon the cylinder volt-ampere characteristics, the theoretical development outlined in the following pages was carried out, and graphs of the predicted cylinder volt-ampere characteristics for selected probe velocities and orientations are displayed. It should be emphasized that the accuracy of the ion density data obtained from experimental curves depends in large part upon the validity of this theory; however, as will be discussed later, the electron temperature and density measurements are not significantly perturbed by probe motion, since the electron current characteristic is essentially unaffected.

Basic considerations.—When a cylindrical collector of very small radius, r, is immersed in a plasma consisting of positive ions and electrons having Maxwellian velocity distribution, it becomes surrounded by a positive-ion sheath of large radius, a, such that the ion current to the collector is functionally independent of a/r.[7] The ion current collected under this condition is termed orbital-motion limited. On the other hand, the electron current to the collector is inherently independent of the sheath dimensions and functionally depends only upon the potential across the sheath and the characteristic properties of the plasma, such as temperature, density, and ion mass. These two cases of current collection constitute the topic of this section. As mentioned earlier, work is being continued toward preparing a separate report which will contain the detailed theoretical study of current collection of moving cylindrical probe for all probe sizes. Therefore, for the purpose of avoiding the repetition of mathematical steps involved in arriving at the desired current functions for a small cylinder, only the final results are given conjointly with some discussion of the essential physics behind the corresponding current functions.

2.1.2. The General Current Functions.—Consider a cylinder of length L and radius r ($L \gg r$) moving in the plasma with drift velocity W. Let θ be the angle between the axis of the cylinder and the velocity vector W. Assume that the sheath is a circular cylinder concentric with the collector and that the sheath retains its cylindrical shape at all drift velocities of the probe. Considering the particles of one particular sign, let N be the number per unit volume. In a plane normal to the axis of the cylinder let u_x be the radial and p the tangential velocity components of a particle with respect to the moving system; u_x and p being positive when directed toward the collector. Since the Maxwellian distribution with respect to the stationary probe is modified when the probe is moving, the current reaching the collector is dependent on the angle of orientation θ. If C_m represents the most probable velocity of the particles defined as $C_m = \sqrt{2kT/m}$, and $\kappa = \lambda \sin\theta$, where $\lambda = W/C_m$, then the total current reaching the cylindrical collector may be expressed as

$$I = 2LaNeC_m e^{-\kappa^2} \int_{0,u_1}^{\infty} \int_{-p_1}^{p_1} \exp\left[-\left(\frac{u_x^2+p^2}{C_m^2}\right)\right] I_0\left(2\kappa\sqrt{\frac{u_x^2+p^2}{C_m^2}}\right) \frac{u_x}{C_m}\, d\left(\frac{u_x}{C_m}\right) d\left(\frac{p}{C_m}\right) \tag{1}$$

where I_0 is the modified Bessel function of order zero. Here the lower limit of u_x is to be taken zero when the collector potential is accelerating, and u_1 when retarding.

The limits of integration and the sign convention.—The limits u_1 and p_1 are obtained by applying the laws of conservation of energy and angular momentum as follows.

Let a particle of either polarity (±e) enter the sheath about a collector of either polarity (±V). If p, u_x represent the tangential and the radial velocity components of that particle at the sheath surface in a plane normal to the cylinder axis, respectively, and p_0, u_0 the corresponding quantities at any intermediate point in the sheath; then from the laws of conservation of energy and angular momemtum we have the following balance:

$$p^2 + u_x^2 = p_0^2 + u_0^2 + 2\,\frac{(\pm e)(\pm V)}{m} \tag{2a}$$

$$ap = \rho p_0 \tag{2b}$$

where m is the mass of the particle, a is the radius of the sheath and ρ is the radial distance of the intermediate point from the axis of the cylinder. Substitute for p_0 in (2a) from (2b) to obtain

$$p^2\left(\frac{a^2-\rho^2}{\rho^2}\right) + u_0^2 - u_x^2 + 2\,\frac{(\pm e)(\pm V)}{m} = 0\ . \tag{3a}$$

For the particle to reach the collector, its magnitude of velocity at the collector must be equal to or larger than zero i.e., $u_0^2 \geqslant 0$, otherwise it will miss the collector. Also, at the sheath surface the particle should be proceeding in the direction of the collector, which means $u_x > 0$. Using these conditions in (3a) and replacing ρ by r, the collector radius, and p by p_1, we obtain after rearrangement of the terms the following:

$$p_1^2 = \frac{r^2}{a^2-r^2}\left[u_x^2 - 2\,\frac{(\pm e)(\pm V)}{m}\right]. \tag{3b}$$

Now let us examine Eq. (3b) in conjunction with the energy balance equation given by (2a) using specific examples. Consider a positive ion (+e) entering the sheath when the collector potential is negative (-V) with respect to plasma. Essentially, the positive ion will gain energy due to acceleration during its passage in the sheath towards the collector, which means that its kinetic energy in the sheath is larger than that at the sheath edge. But the law of conservation energy demands an energy balance, hence we must subtract the amount of energy gained in the sheath, which is $\left|\frac{2eV}{m}\right|$, from the right hand side of (2a). On the other hand, when an electron enters the sheath about the negative collector, it loses energy, and thus in order to compensate for the lost energy one must add that amount, which is lost, to the right hand side of (2a). Mathematically we can achieve this by retaining the polarities of the particles and the collector potentials. Thus in the case of a positive ion (+e) encountering a negative collector potential (-V) the trajectory relation (3b) becomes

$$p_1^2 = \frac{r^2}{a^2-r^2}\left(u_x^2 + \frac{2eV}{m}\right) \tag{3c}$$

and in the case of an electron (-e) and the same negative collector potential we have

$$p_1^2 = \frac{r^2}{a^2-r^2}\left(u_x^2 - \frac{2eV}{m}\right). \tag{3d}$$

Also, the least radial velocity u_1 required for the electron to reach the collector can be easily obtained from (3d) by putting $p_1 = 0$, i.e.,

$$u_1^2 = \frac{2eV}{m} \tag{3e}$$

which is the lower limit to be used in integral (1) for determining the electron current function when the collector is negative.

Normalization of the current functions.—To visualize the effects of the sheath upon the current collection, it is convenient to introduce the concept of a normalized current, I_n, which is simply the collected current divided by the current which would have resulted without the sheath. This is given by

$$I_n = \frac{I}{\sqrt{\frac{kT}{2m\pi}}\, NeA_c} \tag{4}$$

where A_c is the collector area.

The general current function for accelerating potential.—In order to obtain the orbital-motion-limited current, $a/r \to \infty$, apply L'Hospital's to the integral (1) and then integrate with zero as the lower limit of u_x. The final result in the normalized form, as given by (4), is

$$I_n = e^{\bar{V}-\kappa^2} \sum_{n=0}^{\infty} \frac{(2n+1)!}{(n!)^2 2^{2n}} \left[\left(\frac{\kappa}{\sqrt{\bar{V}}}\right)^n J_n(2\kappa\sqrt{\bar{V}}) - (-1)^n \left(\frac{\sqrt{\bar{V}}}{\kappa}\right)^{n+\frac{3}{2}} J_{n+\frac{3}{2}}(2\kappa\sqrt{\bar{V}}) \right] \tag{5}$$

where $\bar{V} = eV/kT$, a normalized potential, J_n, is the cylindrical Bessel function of index n and $J_{n+\frac{3}{2}}$ is the spherical Bessel function of index $n+3/2$. Equation (5), therefore, represents the normalized current to the collector when V is accelerating; for instance, the ion current when the collector is negative with respect to the plasma, or the electron current when the collector is positive.

When $\kappa = 0$, (5) reduces to

$$I_n\Big|_{\kappa\to 0} = \frac{2}{\sqrt{\pi}}\left[\sqrt{V} + \frac{2}{\sqrt{\pi}}\, e^{V}\, \mathrm{erfC}\,(\sqrt{V})\right] \tag{6}$$

where erfC is the complimentary error function. Since $\kappa = \lambda\sin\theta$, Eq. (6) implies two situations: either $\lambda = 0$, the probe is stationary, or $\theta = 0$, the collector is pointing axially in the direction of the velocity vector W. In both cases, therefore, there is no effect of the drift velocity on the collected current.

For values of $|V| \gg 1$, Eq. (6) can be approximated by the simpler expression, which is the same result given by Langmuir[7] for a stationary cylindrical probe.

$$I_n\Big|_{\kappa\to 0} \simeq \frac{2}{\sqrt{\pi}}\sqrt{1 + V}\,. \tag{7}$$

<u>The general current function for retarding potential.</u>—In the case of retarding potential, the current function is obtained by integrating (1) with the lower limit u_1 as given by relation (3e). The result in normalized form is

$$I_n = e^{-(V+\kappa^2)} \sum_{n=0}^{\infty} \frac{(2n+1)!}{(n!)^2 2^{2n}} \left(\frac{\kappa}{\sqrt{V}}\right)^n I_n(2\kappa\sqrt{V}) \tag{8}$$

where $I_n(2\kappa\sqrt{V})$ is the modified Bessel function of order n, which is not to be confused with the subscript of the normalized current I_n.

If we consider the current to a stationary collector, the current function (8) reduces to a simpler form (by putting $\kappa = 0$) as given by

$$I_n\Big|_{\kappa\to 0} = e^{-V}\,. \tag{9}$$

Equation (8), or its zero velocity from (9), is inherently independent of the sheath radius but depends upon the only unknown variable $\overline{V}$, thus permitting direct interpretation of the retarded current in terms of the temperature of the particles.

2.1.3. The Electron and Ion Current Functions.—Since in practice Langmuir probe characteristics are usually interpreted in the voltage range which is negative with respect to the plasma, we will present the current characteristics for this range only; thus, we need consider only the accelerated ion current and the retarded electron current. For ions, the effects of probe motion are only negligible near the apogee of the rocket trajectory, and Eq. (5), containing the drift velocity, must normally be used for ions. However, the electron velocities always exceeds probe velocities and Eq. (9) holds to a very close approximation.

The resulting ion current function obtained from the accelerating case (5) and Eq. (4) is given by

$$I_p = \sqrt{\frac{kT_p}{2m_p\pi}}\, N_p e A_c I_n \qquad (10)$$

where the subscript p designates the positive ion parameters. The corresponding electron current function is obtained by combining the retarded current Eq. (9) and the definition (4).

$$I_e = \sqrt{\frac{kT_e}{2m_e\pi}}\, N_e e A_c I_n \Big|_{\kappa\to 0} \qquad (11)$$

where the e refers to the electron parameters.

With these equations we are equipped to accomplish the objective of this theoretical study, namely, the prediction of volt-ampere characteristics and the reduction of ionosphere parameters from experimental characteristics.

2.1.4. Predicted Volt-Ampere Characteristics of the Cylinder.—In obtaining the current characteristics from Eqs. (10) and (11), given in the previous section, we parameterize for various angles of orientation $\theta = 0°$, $45°$, $90°$ and select λ for ions as 0, 1, 2, $\lambda = 0$ for electrons, $T = 1600°K$ and $N = 10^5$ ions/cc. Figure 4 illustrates the stationary probe characteristic, $\lambda = 0$, in which the net current is drawn versus the applied difference of potential δV between the collector and the 8-inch perforated sphere. Since, here, $\lambda = 0$ there is no orientation effect. Figure 5 is drawn for $\lambda = 1$ and the range of θ as shown. Here, as one would expect, the orientation effect is visible mostly in the positive ion current region. Figure 6 demonstrates the similar behavior at higher probe velocity, $\lambda = 2$, where the orientation effect is more pronounced.

Ion density.—In reducing the ion density from experimental data, it is evident from Figs. 5 and 6 that the effects of orientation must be considered. Thus, using the measured current, probe velocity, orientation angle, potential, and assumed values of ion temperature and mass, we can determine the ion density from (10).

Electron temperature.—Figure 7 illustrates the entire electron current characteristic for $\lambda = 2$ and all θ. Since the net ion current component for all θ is small compared with the electron current component, the orientation angle has negligible effect on the electron temperature determination. Thus

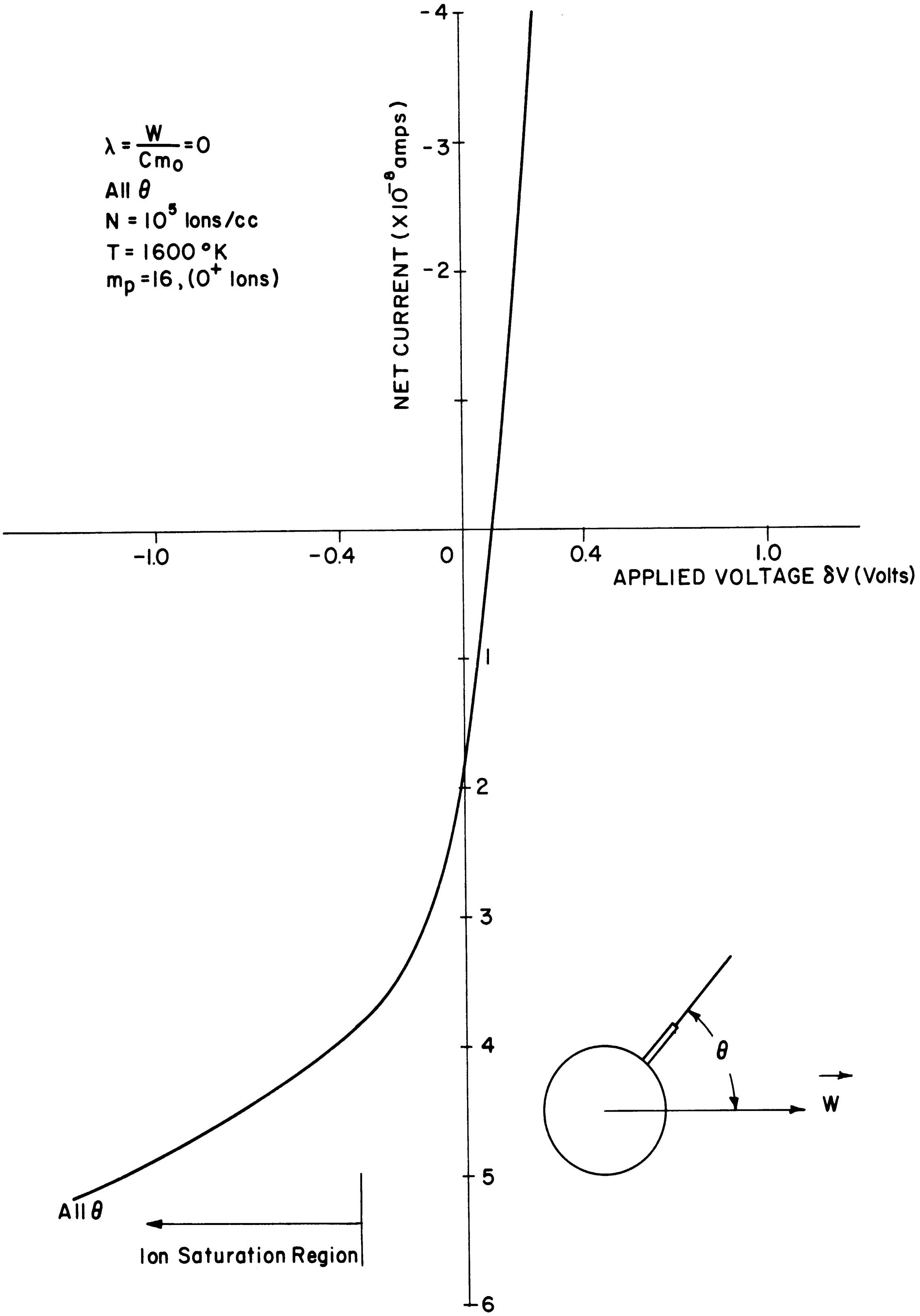

Fig. 4. A predicted volt-ampere characteristic of a stationary thin cylindrical Langmuir probe, under typical F_1 region conditions, showing primarily the ion saturation region of the current characteristic.

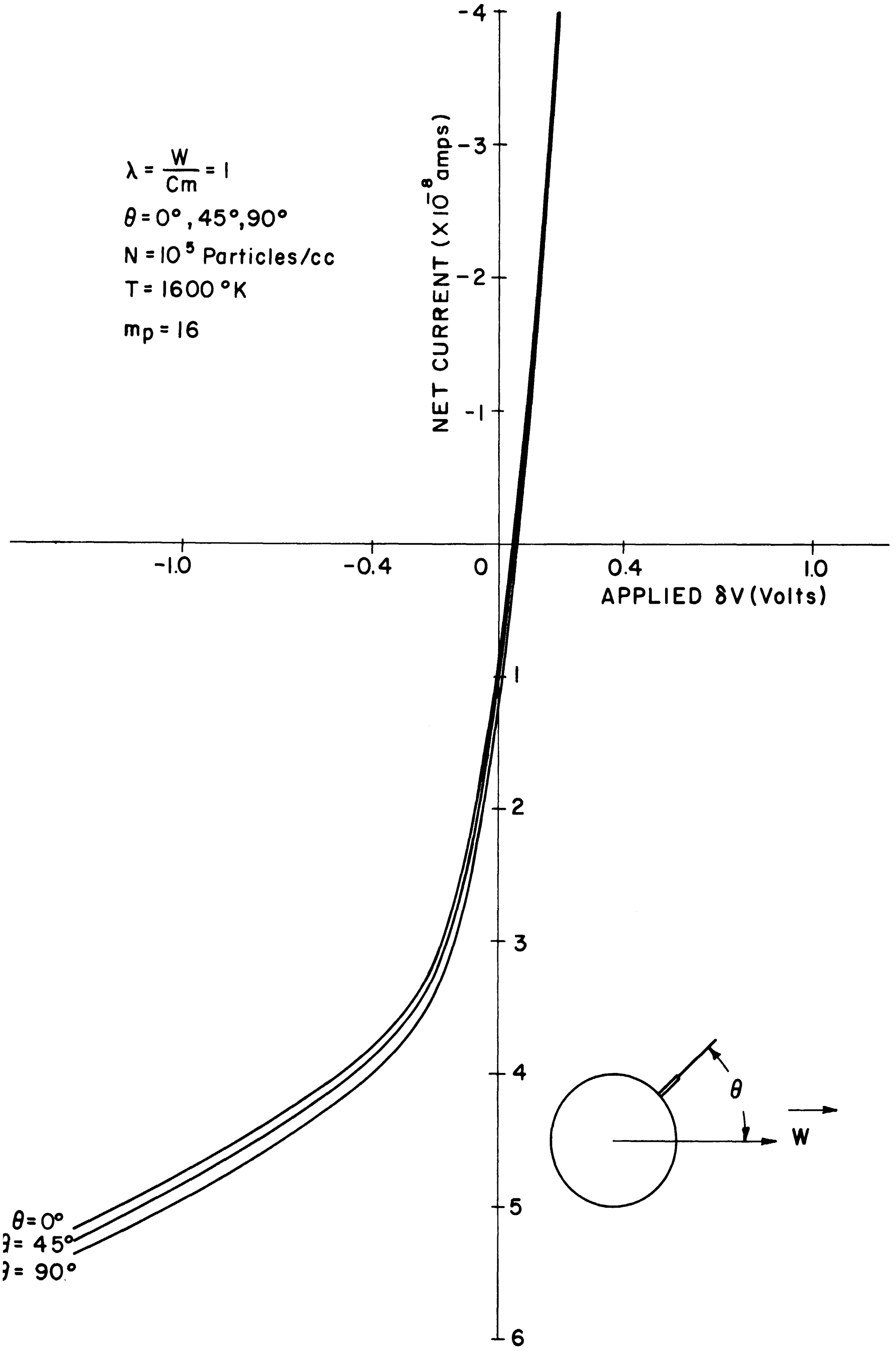

Fig. 5. A predicted volt-ampere characteristic of a cylindrical probe illustrating the effect of orientation upon the ion current characteristic at a fixed velocity ratio, $\lambda = 1$.

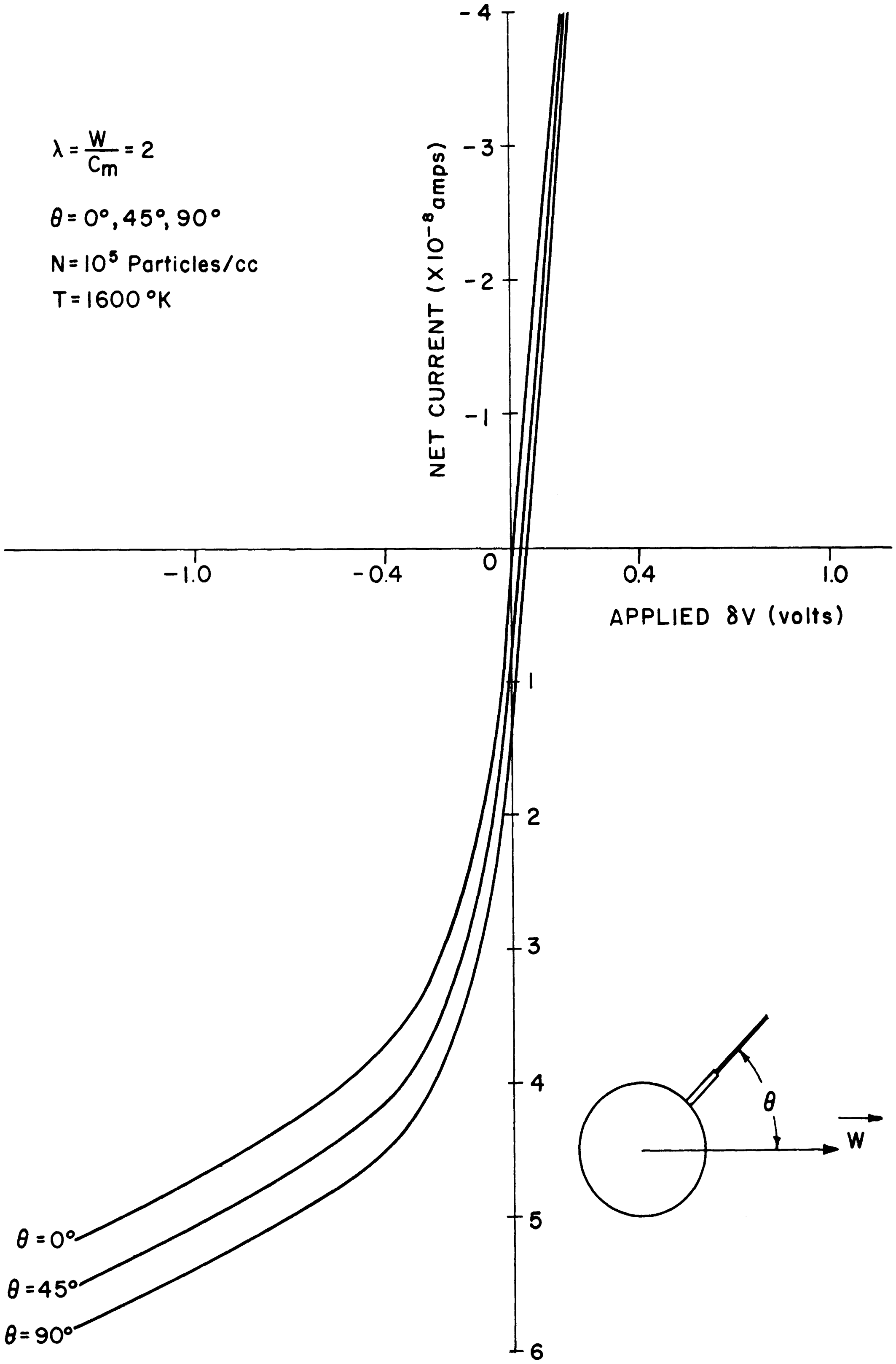

Fig. 6. A predicted volt-ampere characteristic of a cylindrical probe illustrating the effect of probe orientation upon the ion current characteristic at a fixed velocity ratio, $\lambda = 2$.

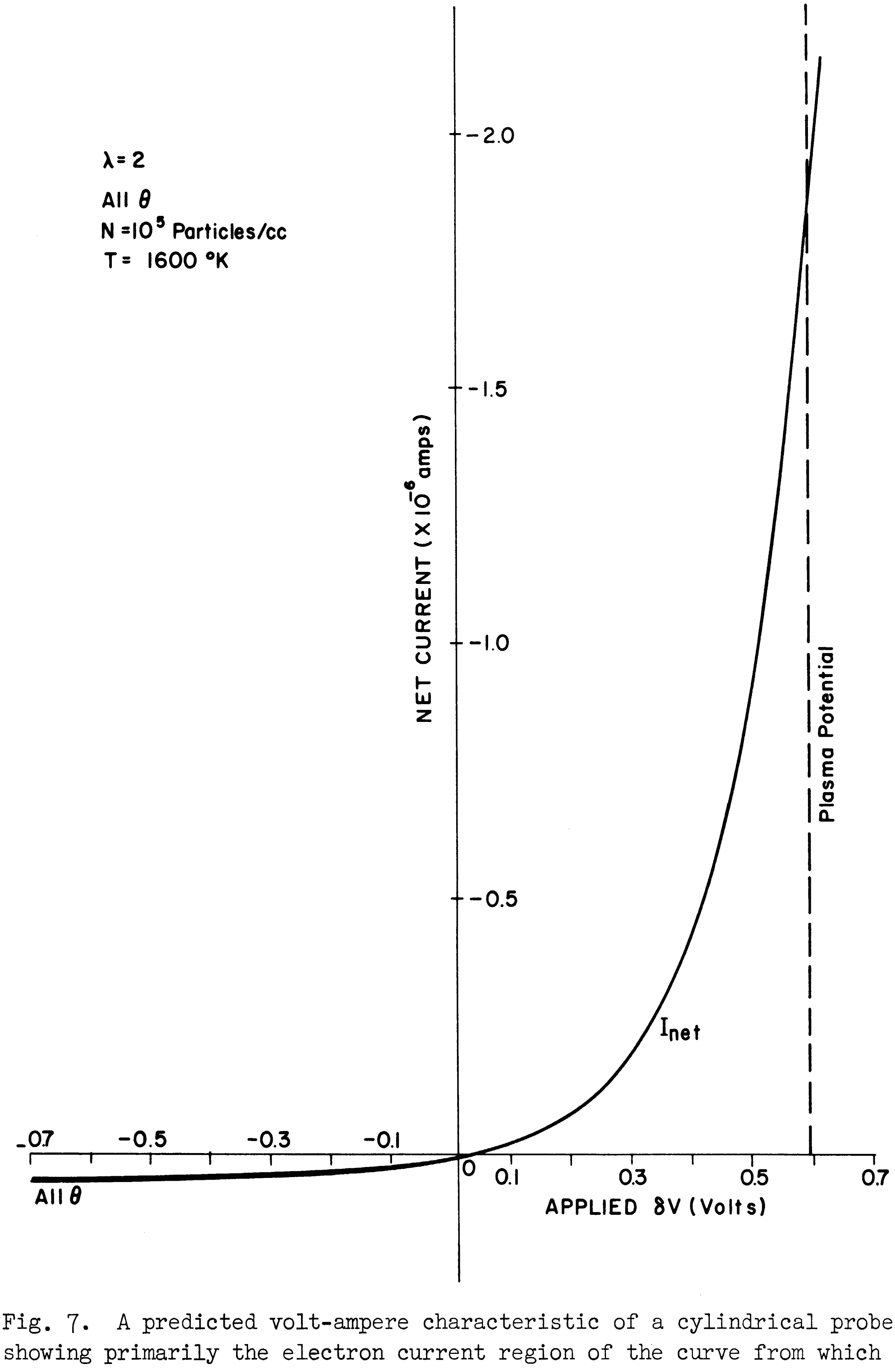

Fig. 7. A predicted volt-ampere characteristic of a cylindrical probe showing primarily the electron current region of the curve from which the electron temperature may be derived.

with the help of Eq. (11) we can determine the electron temperature, by plotting the log of electron current versus the applied voltage. Mathematically the electron temperature is given by

$$\frac{d}{d\delta V} [\log_e I_e] = \frac{e}{kT_e} . \qquad (12)$$

2.2. THE SPHERICAL ION TRAP

2.2.1. Introduction.—Figure 8 is a simplified block diagram of the 8-inch sphere, connected in its ion trap mode of operation. In this mode the perforated sphere, of radius r_g, is connected to the inner sphere, of radius r_c, through a current detector, I, and the sawtooth voltage generator, V_a, while the Langmuir probe is disconnected electrically and allowed to float in the plasma. Unlike the ion trap used by the Russians on Sputnik III[8] in which the perforated sphere or grid was swept through a range of potentials with the spacecraft as reference, the grid used here is the reference electrode. Its potential is established by the electron temperature and the ion-to-electron mass ratio in the plasma. In operation, the inner sphere is swept through a suitable range of potentials such that, at the negative extreme, all ions entering the holes in the 8-inch sphere are collected by the inner sphere and all electrons are rejected; and, at the positive extreme, all electrons are collected and the ions rejected. The theoretical development outlined in the following pages has provided current equations from which the volt-ampere characteristics of the ion trap may be predicted and with which experimental characteristics can be reduced to the ionosphere parameters of electron and positive ion temperatures and densities.

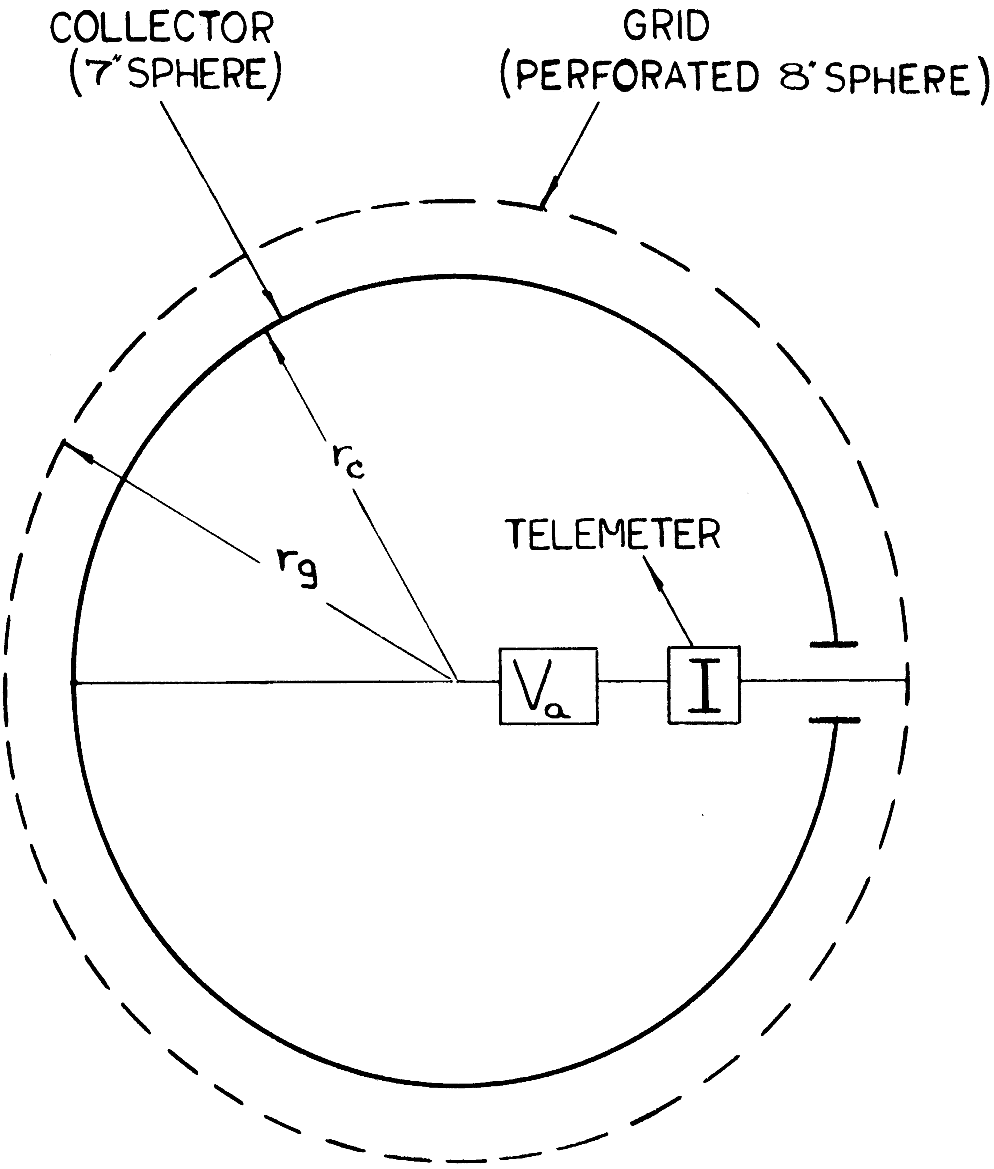

Fig. 8. Simplified block diagram of the 8-inch sphere shown in its ion trap mode of operation.

2.2.2. General.—Success of this development when used in conjunction with the experimental data for reducing the ion temperature is dependent upon validity of the following assumptions: (1) the medium in which the probe moves is characterized by the Maxwellian velocity distribution of the particles, (2) the spherical shape of the sheath is retained even at velocities which exceed the most probable velocity of the ions by an appreciable factor, (3) the grid collector field does not extend appreciably beyond the boundary of the grid surface, thus only the charged particles that enter the holes experience the field, and (4) the holes in the grid surface are sufficiently large in number, and randomly distributed that the current reaching the collector is independent of instrument orientation and thus can be represented as a fraction η of the total current to the grid; η being the ratio of the total hole area to the entire area of the 8-inch sphere.

The validity of assumption (2) is highly questionable when the probe velocity approaches or exceeds the most probable velocity of the ions. However, no sufficiently precise development is available which will predict a specific sheath configuration as a function of the drift velocity or justify empirically any other shape. For this reason, and because of its inherent simplicity, a spherical sheath is assumed. As for the assumptions (3) and (4), the probe design and its range of operation allow us to incur these simplifying assumptions, particularly in regard to the extension of the collector-grid field outside the holes. A simple field mapping experiment, simulating the 8-inch ion trap probe, performed in this laboratory, dictated the size and number of holes for a minimal field protrusion and acceptable grid transparency, which is of the order of 12%.

Plan of the following sections.—Since the object of this section is to introduce the expected volt-ampere characteristics of the 8-inch ion trap experiment, it is considered desirable here to defer the detailed theoretical analysis for a separate report to be published in the near future. We will discuss only the most significant physical basis of the theory which lead us to the corresponding current functions in the following sequence.

Assuming that the velocity distribution of the particles constituting the plasma is Maxwellian and that thermal equilibrium exists, we will first examine the allowed distribution of the ion and electron velocities at the grid surface when these particles have fallen through the potential across the sheath. This will be followed by the study of a new parameter, the thickness of the grid, t, and its possible inhibiting effects on the current collection when the applied potential is accelerating and retarding for ions and electrons. This should establish enough background for grasping the physical meaning of the current functions together with the volt-ampere characteristics given on pages 47.

Allowed velocity domains of ions and electrons at the grid surface.—In order to find the allowed velocity domains of the charged particles at the grid surface we must consider the way in which the radial and the tangential velocity components transform from the sheath edge to the grid surface in the usual case when the wall potential of the grid is negative $(-V_W)$ with respect to the plasma such that the ions are accelerated and the electrons are retarded.

Let a be the radius of the sheath and r_g the radius of the grid. If u_s and p_s are the radial and the tangential velocity components of a charged particle at the sheath edge with respect to the moving system, and u_g and p_g are the corresponding components of velocity at the grid surface, as shown in Fig. 9, then from the laws of conservation of energy and angular momentum,

$$p_s^2 + u_s^2 = p_g^2 + u_g^2 + 2\,\frac{(\pm e)(-V_W)}{m} \tag{13}$$

$$p_s = \frac{r_g}{a}\,p_g\ . \tag{14}$$

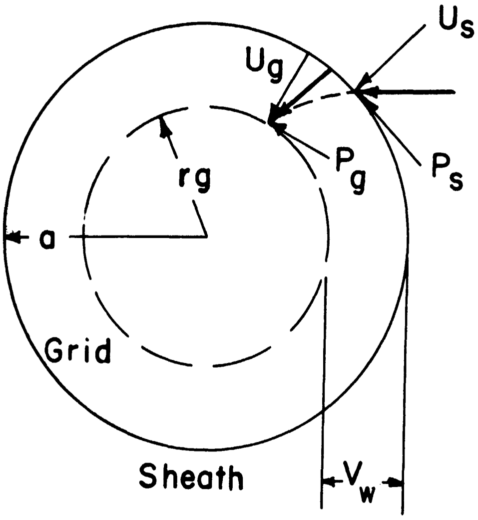

Fig. 9. Trajectory of a positive ion in the sheath.

These equations hold for both ions and electrons and for both positive or negative grid potentials, however care must be exercised in selecting the proper sign, of e, as was done in the case of cylindrical collector.

Thus (13) and (14) provide the necessary functional relations for transforming the velocity components from the sheath edge to the grid surface.

Ions.—Further consideration of the above relations suggests that, at the grid surface, certain values of u_g and p_g are excluded for positive ions. In fact, the only points in the u_g, p_g plane which correspond to real values of u_s and to positive values of u_g (both of which are necessary for the ion to reach the grid) are those lying to the right of the p_g axis and outside the ellipse given by

$$\frac{p_g^2}{[a^2/a^2-r_g^2]} + u_g^2 - \frac{2eV_W}{m} = 0 \tag{15}$$

the region shown hatched in Fig. 10. We see then that, with an accelerating potential on the grid, the Maxwellian nature of the distribution is not completely obliterated as the ions move into the sheath. At any point certain whole groups of ions proper to a Maxwellian distribution are absent, but the remaining ions have precisely the distribution which is characteristic of a complete Maxwellian distribution represented by the same temperature as that of the ions at the sheath boundary, with due consideration to the drift velocity of the system. Furthermore, the space density of ions in each velocity class, outside the excluded one, satisfies Boltzmann's relation.

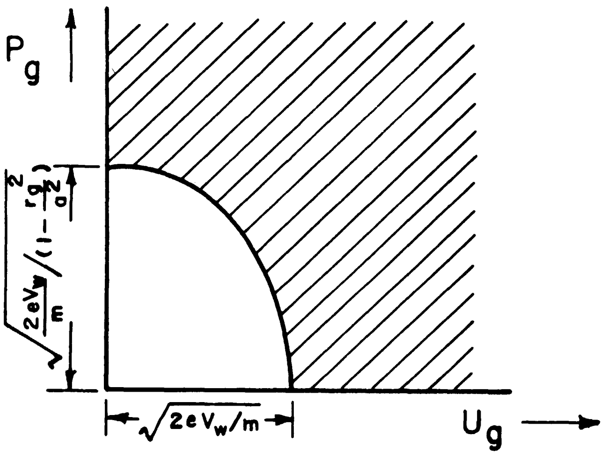

Fig. 10. Velocity domain of positive ions at the grid surface.

Electrons.—In the case of electrons, however, the entire character of the distribution is Maxwellian, as can be seen from the transformation equations (13) and (14), in which all points in the u_g, p_g plane correspond to real values of u_s, i.e.,

$$\frac{p_g^2}{[a^2/(a^2-r_g^2)]} + u_g^2 = 0 \qquad (16)$$

constituting the entire region shown shaded in Fig. 11. Hence with a retarding potential on the grid the Maxwellian nature of the distribution is completely retained at the grid surface.

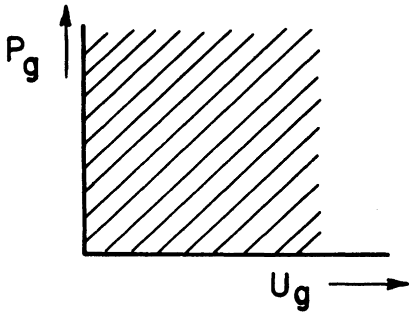

Fig. 11. Velocity of electrons at the grid surface.

Effect of grid thickness and hole diameter on current collection.—In considering the current to the collecting 7-inch sphere, the permitted u_g, p_g domains shown in Figs. 10 and 11, are further modified in a way depending upon, (1) the grid thickness, t, and hole diameter, d, as shown in Fig. 12, and (2) the applied potential V_a between the collector and the grid. The probability of collecting a particle, which has entered any grid hole, is determined by its trajectory in the grid-collector space, as expressed through the relation

$$p_{1g}^2 = \gamma_o^2 \left[u_g^2 - 2 \frac{(\pm e)(\pm V_a)}{m} \right] \qquad (17)$$

where p_{1g} is the tangential velocity component at the hole for which the collection of the particle for all u_g, the radial component is plausible, $\gamma_o^2 = r_c^2/(r_g^2-r_c^2)$, a design constant, r_c, being the radius of the collector, r_g, the radius of the grid, and V_a is the applied potential between the collector and the grid. If we then define a certain limiting angle, θ_ℓ, as

$$\tan \theta_\ell = \frac{p_{1g}}{u_g} = \gamma_o \sqrt{1 - 2 \frac{(\pm e)(\pm V_a)}{m u_g^2}} , \qquad (18)$$

we conclude that for a given particle, the allowed range of θ_ℓ is determined by the range of u_g, and the magnitude and polarity of V_a and the polarity of the particle. Let ϕ be the half angle of the cone, as shown in Fig, 12, such that

$$\tan \phi = \frac{d}{t} . \qquad (19a)$$

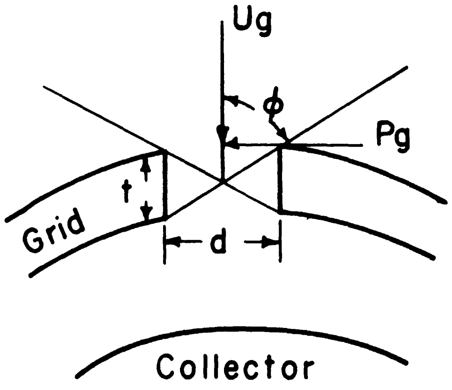

Fig. 12. Half angle of the acceptance cone due to grid thickness and hole size.

Now examine Eq. (18) in conjunction with the design angle ϕ as defined by (19a).

We know that no particle travelling in a straight line can physically cross the hole freely if its angle to the normal is greater than ϕ. Then, for a given V_a, if θ_ℓ can assume values that are larger than ϕ, the grid thickness inhibits the collection. If θ_ℓ cannot assume values that are larger than ϕ for the entire range of u_g and a given V_a, then the grid thickness has no inhibiting effect on the collection. In the following sections, we will see that the latter is always true for the particles that are retarded by the collector if and only if $\gamma_o < \tan \phi$. The physical dimensions of the 8-inch ion-trap probe are such that

$$\gamma_o \cong 1.8$$

and

$$\tan \phi \cong 6.25, \qquad (\phi \doteq 81°)$$

hence

$$\gamma_o \ll \tan \phi \ .$$

Thus no grid thickness effect should be expected for the retarded current to the collector.

We will now take a specific case of ion current collection when V_a is accelerating and apply the above conclusions and the allowed velocity domain of the ions at the grid surface to demonstrate, graphically, that even for accelerating V_a the grid thickness has no effect on the current collector for a certain range of V_a.

2.2.3. The Ion Current for Accelerating Applied Voltage (V_a negative).— Consider the trajectory relation for ions as given by Eq. (17) with a proper designation of the signs

$$p_{1g}^2 = \gamma_o^2 \left(u_g^2 + \frac{2eV_a}{m} \right) . \qquad (19b)$$

If we plot Eq. (19b) with u_g, p_g in rectangular coordinates, we obtain a hyperbola whose vertex on the positive p_g axis is $\gamma_o(2eV_a/m)^{1/2}$, as shown in Fig. 13. Also from Fig. 10 the semi-major axis of the ellipse on the positive p_g axis is $\tau(2eV_w/m)^{1/2}$, where $\tau = [a^2/(a^2-r_g^2)]^{1/2}$. Superimposition of the two figures, shown hatched in Figs. 14 and 15, yields the resultant allowed energy domain of the ions. Here, tan ω is defined as the slope of the line drawn through the point of intersection of the two curves. Now two conditions arise when a line with a slope tan ϕ is drawn, (1) when tan $\omega >$ tan ϕ, the resulting allowed energy domain of ions becomes as shown hatched in Fig. 14, from which it is clear that the grid thickness bears some inhibiting effect on the ion current collection, and (2) when tan $\omega <$ tan ϕ, the allowed energy domain remains unaltered as shown hatched in Fig. 15, thus indicating no inhibiting effect of the grid thickness on the ion current collection.

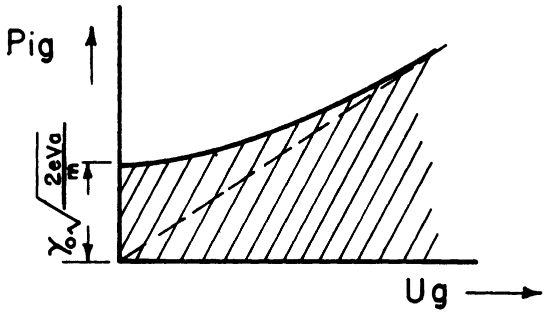

Fig. 13. Plot of the trajectory relation for ions in the grid-collector space when the applied voltage is accelerating.

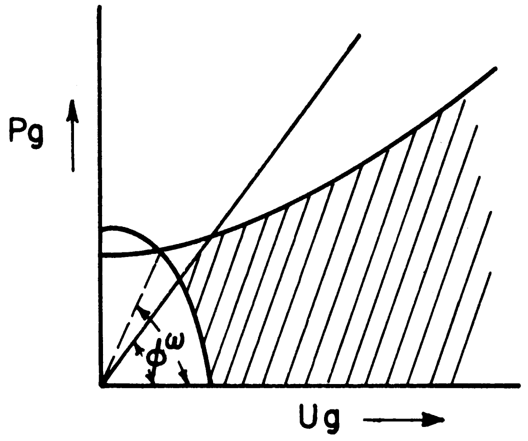

Fig. 14. Resultant domain of the ion velocities for collection with grid thickness effect when the applied voltage is accelerating.

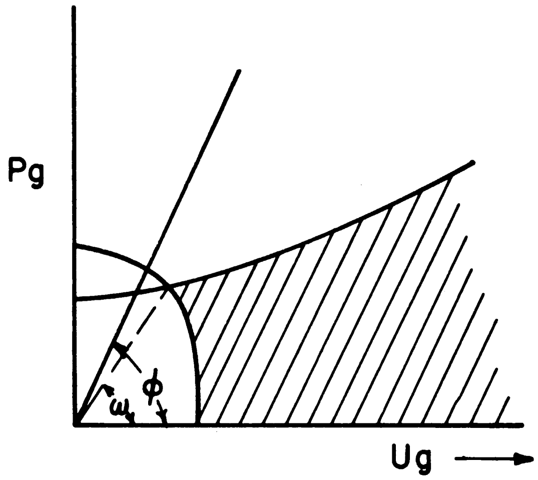

Fig. 15. Resultant domain of the ion velocities for collection with no grid thickness effect when the applied voltage is accelerating.

We, therefore, conclude that the transition from grid thickness effect to no effect, or vice versa, occurs at $\omega = \phi$. In terms of the physical parameters, the transition occurs when

$$\frac{V_a}{V_w} = \frac{\tau^2(\tan^2\phi - \gamma_o{}^2)}{\gamma_o{}^2(\tan^2\phi + \tau^2)} \tag{20a}$$

where V_w is the equilibrium potential across the sheath as defined before.

Therefore, for accelerated ion current there are two different current functions corresponding to operation above or below the voltage ratio given by (20a). Thus, when the applied voltage is such that

$$\frac{V_a}{V_w} < \frac{\tau^2(\tan^2\phi - \gamma_o{}^2)}{\gamma_o{}^2(\tan^2\phi + \tau^2)}\ , \tag{20b}$$

the ion current function for accelerating V_a is given* by

$$I_i = \eta\sqrt{\frac{kT}{2m\pi}}\,NeA_c\left[\frac{a^2}{r_c^2}\Lambda(\lambda) - \left(\frac{r_g^2}{r_c^2}\sin^2\phi - 1\right) H\left(\sqrt{\bar{V}_a\Big/\left(\frac{r_g^2}{r_c^2}\sin^2\phi - 1\right) - \bar{V}_w}\,,\ \lambda\right)\right.$$

$$\left. - \left(\frac{a^2}{r_c^2} - \frac{r_g^2}{r_c^2}\sin^2\phi\right) H\left(\sqrt{\bar{V}_w r_g^2 \sin^2\phi/(a^2 - r_g^2\sin^2\phi)}\,,\ \lambda\right)\right] \tag{21}$$

where

$$\lambda = \frac{W}{C_m} = \frac{\text{drift velocity of the probe}}{\text{most probable velocity of the ions}}$$

$C_m = \sqrt{2kT/m}$

$\bar{V}_a = eV_a/kT$, the normalized applied voltage

$\bar{V}_w = eV_w/kT$, the normalized equilibrium potential across the sheath

$$\Lambda(\lambda) = \frac{\sqrt{\pi}}{2\lambda}\left(\lambda^2 + \frac{1}{2}\right)\operatorname{erf}(\lambda) + \frac{1}{2}e^{-\lambda^2} \tag{22}$$

$$H(x,\lambda) = \frac{\sqrt{\pi}}{4\lambda}\left(\lambda^2 + \frac{1}{2} - x^2\right)\left[\operatorname{erf}(x+\lambda) - \operatorname{erf}(x-\lambda)\right]$$

$$+ \frac{x+\lambda}{4\lambda}e^{-(x-\lambda)^2} - \frac{x-\lambda}{4\lambda}e^{-(x+\lambda)^2} \tag{23}$$

η = coefficient of transparency of the grid

A_c = area of the collector.

The H function occurs rather frequently, hence it is defined in (23) for a general argument x.

For the special case of a stationary probe, $\lambda = 0$, Eq. (21) reduces to the simpler form,

---

*Derivation of the current functions is given in a separate report which deals with the detailed theoretical aspects of the 8-inch ion trap probe.

$$I_i\big|_{\lambda\to o} = \eta\sqrt{\frac{kT}{2m\pi}}\,NeA_c\left[\frac{a^2}{r_c^2} - \left(\frac{r_g^2}{r_c^2}\sin^2\phi-1\right)\exp\left\{\overline{V}_w-\overline{V}_a\Big/\left(\frac{r_g^2}{r_c^2}\sin^2\phi-1\right)\right\}\right.$$
$$\left.-\left(\frac{a^2}{r_c^2} - \frac{r_g^2}{r_c^2}\sin^2\phi\right)\exp\left\{-\overline{V}_w r_g^2\sin^2\phi/(a^2-r_g^2\sin^2\phi)\right\}\right] \qquad (24)$$

where the symbols have their usual meaning.

On the other hand, when the applied voltage is such that

$$\frac{V_a}{V_w} < \frac{\tau^2(\tan^2\phi-\gamma_o^2)}{\gamma_o^2(\tan^2\phi+\tau^2)} \qquad (20b)$$

the ion current function for accelerating V_a is given by

$$I_i = \eta\sqrt{\frac{kT}{2m\pi}}\,NeA_c\left[\frac{a^2}{r_c^2}\Lambda(\lambda) - \frac{a^2-r_c^2}{r_c^2}H\left(\sqrt{(\overline{V}_w+\overline{V}_a)r_c^2/(a^2-r_c^2)}\right)\right] \qquad (25)$$

where Λ and H functions are defined by (22) and (23), respectively, for their arguments. Since there can be no discontinunity in the current under condition (20a), either of the two current functions, (21) and (22), is valid. For a stationary probe Eq. (25) reduces to the simpler form

$$I_i\big|_{\lambda\to o} = \eta\sqrt{\frac{kT}{2m\pi}}\,NeA_c\left[\frac{a^2}{r_c^2} - \frac{a^2-r_c^2}{r_c^2}\exp\left\{-(\overline{V}_w+\overline{V}_a)r_c^2/(a^2-r_c^2)\right\}\right]. \qquad (26)$$

Thus, it is apparent from the existence of ϕ in (21) that for small applied voltages the ion current is a function of grid thickness and hole diameter. Similarly, the absence of ϕ in Eq. (25) shows the ion current independent of ϕ for large applied voltage.

Now we will consider the collection of ion current when the applied voltage retards the ions, (V_a, positive).

2.2.4. <u>The Ion Current for Retarding Applied Voltage</u> (<u>V_a positive</u>).— When the applied potential V_a is retarding, the ions which enter any hole radially will reach the collector if the voltage equivalent of their radial velocity is equal to, or larger than, V_a, as determined by the trajectory relation (17),

$$p_{1g}^2 = \gamma_o^2\left(u_g^2 - \frac{2eV_a}{m}\right). \qquad (27)$$

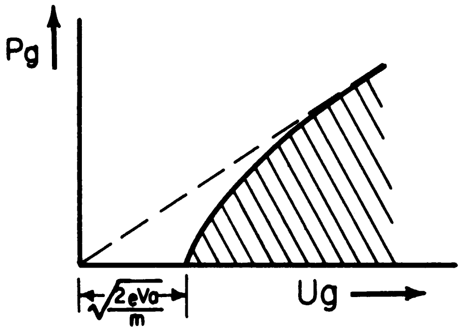

Fig. 16. Plot of the trajectory relation for ions in the grid-collector space when the applied voltage is retarding.

A plot of Eq. (27) yields a hyperbola with a vertex ($\sqrt{2eV_a/m}$, 0) on the u_g axis as shown in Fig. 16. When on this plot the allowed domain of ion velocities at the grid surface, as illustrated in Fig. 10, is superimposed and the ϕ- line drawn, then, depending upon the value of V_a, we have: (1) for $V_a < V_w$, some portion of the hyperbola intersecting the elliptic region as shown in Fig. 17, and (2) for $V_a > V_w$, no portion of the hyperbola intersecting the elliptic region as shown in Fig. 18. Since the asymptote of the hyperbola, as illustrated by the dashed line in Figs. 17 and 18, has a slope of γ_o, and by design $\gamma_o \ll \tan\phi$, the grid thickness bears no effect on the ion current

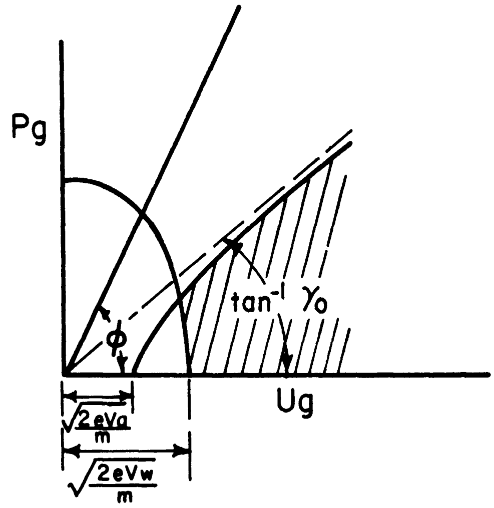

Fig. 17. Resultant domain of the ion velocities for collection when the applied voltage is retarding and $V_a < V_w$.

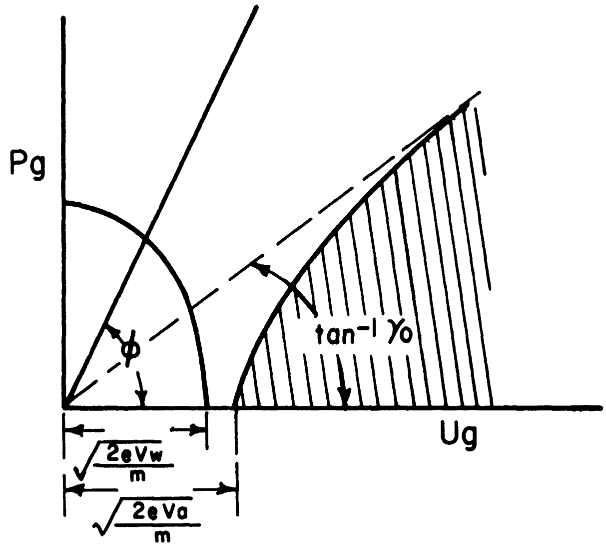

Fig. 18. Resultant domain of the ion velocities for collection when the applied voltage is retarding and $V_a > V_w$.

collection. From Figs. 17 and 18 it is clear that one of two functions represents the ion current, depending upon the value of V_a in relation with V_w, when V_a is retarding. Thus for $V_a < V_w$, the ion current function is given* by

$$I_i = \eta\sqrt{\frac{kT}{2m\pi}}\, NeA_c \left[\frac{a^2}{r_c^2}\Lambda(\lambda) - \frac{a^2-r_c^2}{r_c^2} H\left(\sqrt{(V_w-V_a)r_c^2/(a^2-r_c^2)},\ \lambda\right)\right] \tag{28}$$

where Λ and H functions are again the same as defined by (22) and (23), respectively, and the rest of the symbols have their usual meaning.

For the special case of a stationary probe, (28) reduces to

$$I_i\Big|_{\lambda\to 0} = \eta\sqrt{\frac{kT}{2m\pi}}\, NeA_c \left[\frac{a^2}{r_c^2} - \frac{a^2-r_c^2}{r_c^2}\exp\left\{(V_a-V_w)r_c^2/(a^2-r_c^2)\right\}\right]\cdot \tag{29}$$

---

*See footnote on page 34.

When $V_a > V_w$, the ion current function is given by

$$I_i = \eta\sqrt{\frac{kT}{2m\pi}}\, NeA_c\, H\left(\sqrt{V_a - V_w},\ \lambda\right) \tag{30}$$

which reduces, for the stationary probe, to

$$I_i\Big|_{\lambda\to o} = \eta\sqrt{\frac{kT}{2m\pi}}\, NeA_c\, \exp(V_w - V_a)\,. \tag{31}$$

The ion current, as given by Eq. (30), is independent of the sheath dimensions. This permits the interpretation of ion current in terms of the ion temperature and density without recourse to a second equation relating a/r_g and V_w as was needed for the other ion current functions discussed earlier. We will elaborate on this further when the volt-ampere characteristics are examined. But first the equations for the collection of electron current for accelerating and retarding V_a will be derived in the following section.

2.2.5. The Electron Current for Accelerating Applied Voltage (V_a positive).—Previously we concluded that the allowed velocity domain of electrons at the grid surface covered the entire u_g, p_g plane. When the applied potential is accelerating, collection condition (17) restricts the allowed range to the one covered by the hyperbola. The ϕ-line introduces a further restriction as illustrated by Fig. 19, in which the hatched part now represents the allowed domain. This shows that the grid thickness and hole size eliminates the collection of a certain group of electrons enclosed in the somewhat triangular region of Fig. 19.

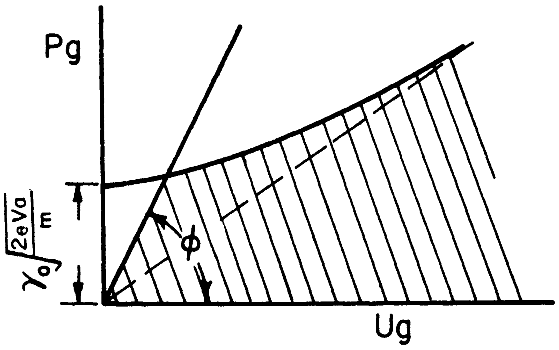

Fig. 19. Resultant domain of the electron velocities for collection when applied voltage is accelerating, $V_a > 0$.

Thus, for accelerated electrons, the current function is

$$I_e = \eta\sqrt{\frac{kT}{2m\pi}}\,NeA_c\left[\frac{r_g^2}{r_c^2}\sin^2\phi\, H(\sqrt{\bar{V}_w},\ \lambda) - \left(\frac{r_g^2}{r_c^2}\sin^2\phi-1\right)\right.$$

$$\left.\cdot\ H\left(\sqrt{\bar{V}_a\Big/\left(\frac{r_g^2}{r_c^2}\sin^2\phi-1\right) + \bar{V}_w},\ \lambda\right)\right] \qquad (32)$$

where H function is defined by (23) and $\bar{V}_a$, $\bar{V}_w$ are the normalized V_a, V_w, respectively.

In the normal use of the 8-inch sphere experiment, the velocity of the probe does not begin to approach the most probable velocity of electrons. Therefore, Eq. (32) can be reduced to a simpler form by letting $\lambda = W/C_m$ approach zero, which results in Eq. (33)

$$I_e\Big|_{\lambda\to 0} = \eta\sqrt{\frac{kT}{2m\pi}}\,NeA_c\, e^{-\bar{V}_w}\left[\frac{r_g^2}{r_c^2}\sin^2\phi - \left(\frac{r_g^2}{r_c^2}\sin^2\phi-1\right)\exp\left\{-\bar{V}_a\Big/\left(\frac{r_g^2}{r_c^2}\sin^2\phi-1\right)\right\}\right] \qquad (33)$$

where the symbols have their usual meaning.

2.2.6. <u>The Electron Current for Retarding Applied Voltage</u> (<u>V_a negative</u>).—This is the simplest of all the cases we have studied. By plotting

Eq. (17) for the retarding potential, and drawing the ϕ-line as shown in Fig. 20, we see that the entire region enclosed by the hyperbola, shown hatched, corresponds to the allowed region for electron collection. As mentioned before, since by design $\gamma_o \ll \tan\phi$, the grid thickness bears no inhibiting effect on the electron current collection. The current function is simply given by:

$$I_e \;=\; \eta\sqrt{\frac{kT}{2m\pi}}\,NeA_c\;H(\sqrt{\bar{V}_a+\bar{V}_w},\;\lambda) \tag{34}$$

where H function is defined by (23) and $\bar{V}_a$, $\bar{V}_w$ are the normalized V_a, V_w, respectively.

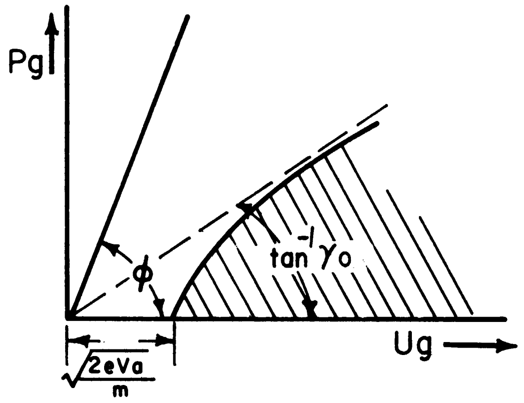

Fig. 20. Resultant domain of the electron velocities for collection when the applied voltage is retarding, $V_a < 0$.

For $\lambda = 0$, which always holds for electrons, Eq. (34) reduces to

$$I_e\Big|_{\lambda\to o} \;=\; \eta\sqrt{\frac{kT}{2m\pi}}\,NeA_c\;\exp[-(\bar{V}_a+\bar{V}_w)]. \tag{35}$$

As one would expect for retarding V_a, the electron current function is independent of the sheath dimension and the dimensions of the collector and the grid. This permits the electron current to be interpreted in terms of the electron temperature by the log plot method described in Section 2.1.4.

2.2.7. Predicted Volt-Ampere Characteristics and Discussion.—In the previous section we have considered the current collection in terms of the applied potential and have arrived at six different current functions: four for ions and two for electrons. In this section we will unify the said functions into complete volt-ampere characteristics.

We start with the assumption that the net current to the collector is the algebraic sum of the ion and electron current components which are considered separately.

Ion component.—Clearly, when V_a is sufficiently negative (the collector negative with respect to the grid), all of the positive ions passing through the holes will be attracted to the collector and the resulting ion current will be essentially independent of changes in V_a. This corresponds to the ion current function (25). At smaller, but still negative values of V_a, some ions which enter the holes will not be collected but will just miss the collector and return to the inner surface of the grid or pass out through another hole on the opposite side from which it entered. This corresponds to a second ion current function for the negative collector, Eq. (21). Clearly, the transition between these two cases occurs at an applied voltage which is a function of the ion trap design parameters such as the grid to collector spacing, hole diameter, and grid thickness.

When the applied potential is positive, a third and fourth ion current function, Eqs. (28) and (30), arise when the V_a is below and above the V_w

through which the ions must fall to reach the grid surface.

Except at extremely high probe velocity, the first three ion current functions (for negative and slightly positive V_a) predict nearly identical currents which are essentially independent of V_a in the range in which they apply. The fourth equation (V_a very positive) contains most of the ion current variation with applied voltage as the ion current falls nearly exponentially from its previously constant value. These four regions are shown in Figs. 22, 23, and 24, for the three velocity ratios, and the equations applicable to each are indicated.

Electron current component.—In contrast to the ion current collection, the electron current functions have only two forms corresponding to an accelerating and retarding V_a, respectively. These are also indicated on the electron current characteristics in the Figs. 22, 23, and 24. Clearly, the net current is given by the algebraic sum of these ion and electron current components.

Application of the equations.—Since the ion current function for the negative collector, given by (21), involves both the sheath radius, a, and the grid wall potential, V_W, which are not independent parameters, we will need an independent relation to solve for the ion current. Solution of the Poisson's differential equation for idealized boundary conditions, such as the zero initial velocity of the ions at the sheath edge, etc., provides one such relation for a stationary probe. However, for high probe velocities we are obliged to discard Poisson's space charge equation and contrive a method which involves a prior assumption of the value of a (or a/r_g) which is consistent with the values of the temperature and density of the medium and then determine the corresponding value of V_w for various λ. The method used is very simple. Let I_{gi} and I_{ge} represent the ion and electron currents to the grid. Then, in the steady state, the net current to the grid must be zero, i.e.,

$$I_{gi} + I_{ge} = 0 . \tag{36}$$

The functional representations of I_{gi} and I_{ge} have been shown to be*

$$I_{gi} = \sqrt{\frac{kT}{2m_i\pi}}\, NeA_g \left[\frac{a^2}{r_g^2}\,\Lambda(\lambda) - \frac{a^2-r_g^2}{r_g^2}\, H\left(\sqrt{\overline{V}_w r_g^2/(a^2-r_g^2)},\ \lambda\right)\right] \tag{37}$$

$$I_{ge} = \sqrt{\frac{kT}{2m_e\pi}}\, NeA_g \exp(-\overline{V}_w)\,; \qquad A_g = 4\pi r_g^2 \tag{38}$$

respectively, where in (37) m_i is the ion mass, in (38) m_e is the electron mass, and Λ and H are defined by (22) and (23), respectively. A combination of (37) and (38) according to (36) yields

$$\frac{a^2}{r_g^2}\,\Lambda(\lambda) - \frac{a^2-r_g^2}{r_g{}^2}\, H\left(\sqrt{\overline{V}_w r_g^2/(a^2-r_g^2)},\ \lambda\right) - \sqrt{\frac{m_i}{m_e}}\exp(-\overline{V}_w) = 0. \tag{39}$$

Then choosing typical values, $a/r_g = 1.1$, $T = 1600°K$ and $\sqrt{m_i/m_e} = 170.5$ we plot (37) and (38) versus $\overline{V}_w$ and find the point of intersection of the two curves. This identifies the normalized equilibrium potential of the grid. This is shown for $\lambda = 0, 1, 2$ in Fig. 21. The corresponding values of $\overline{V}_w$ for the above values of λ are 4.92, 4.66, 4.25, respectively. These values of $\overline{V}_w$

---

*In a previous report M. Kanal has studied these current functions in detail. See Reference (9).

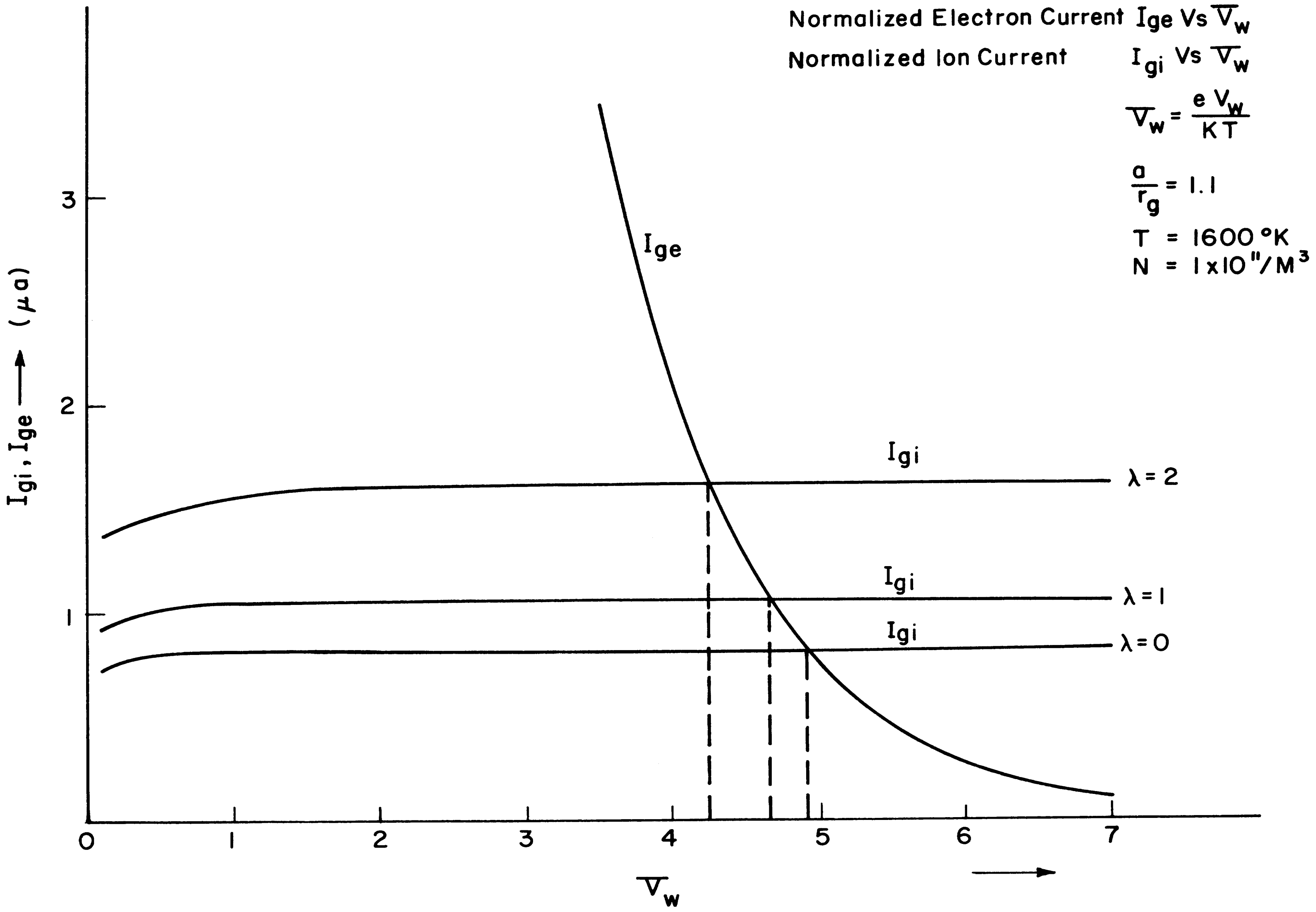

Fig. 21. Graphical solution of Eq. (39) for the net current to the grid for determining the grid wall potential.

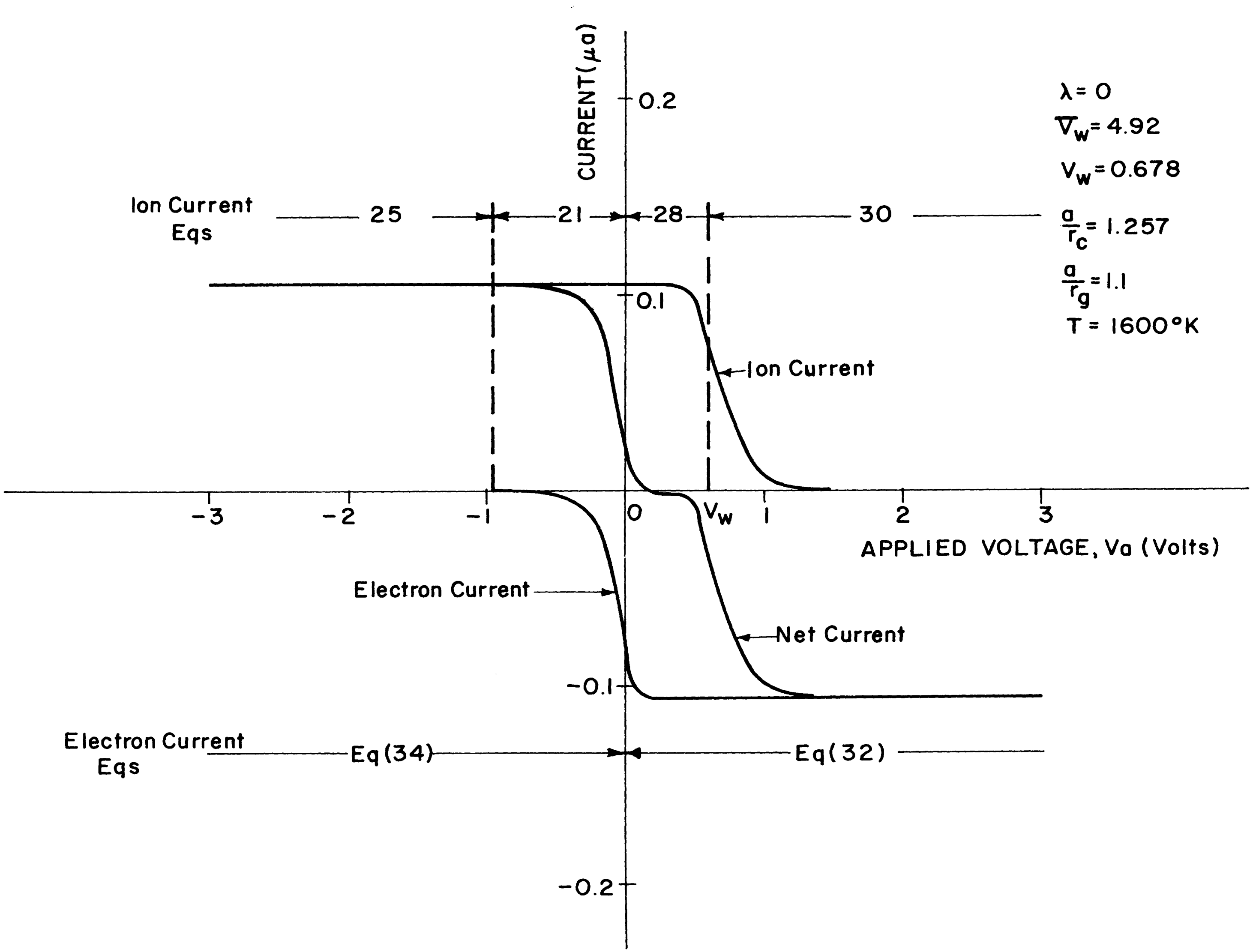

Fig. 22. A predicted volt-ampere characteristic of the 8-inch spherical ion trap which is stationary ($\lambda = 0$). The equations used in obtaining it are indicated.

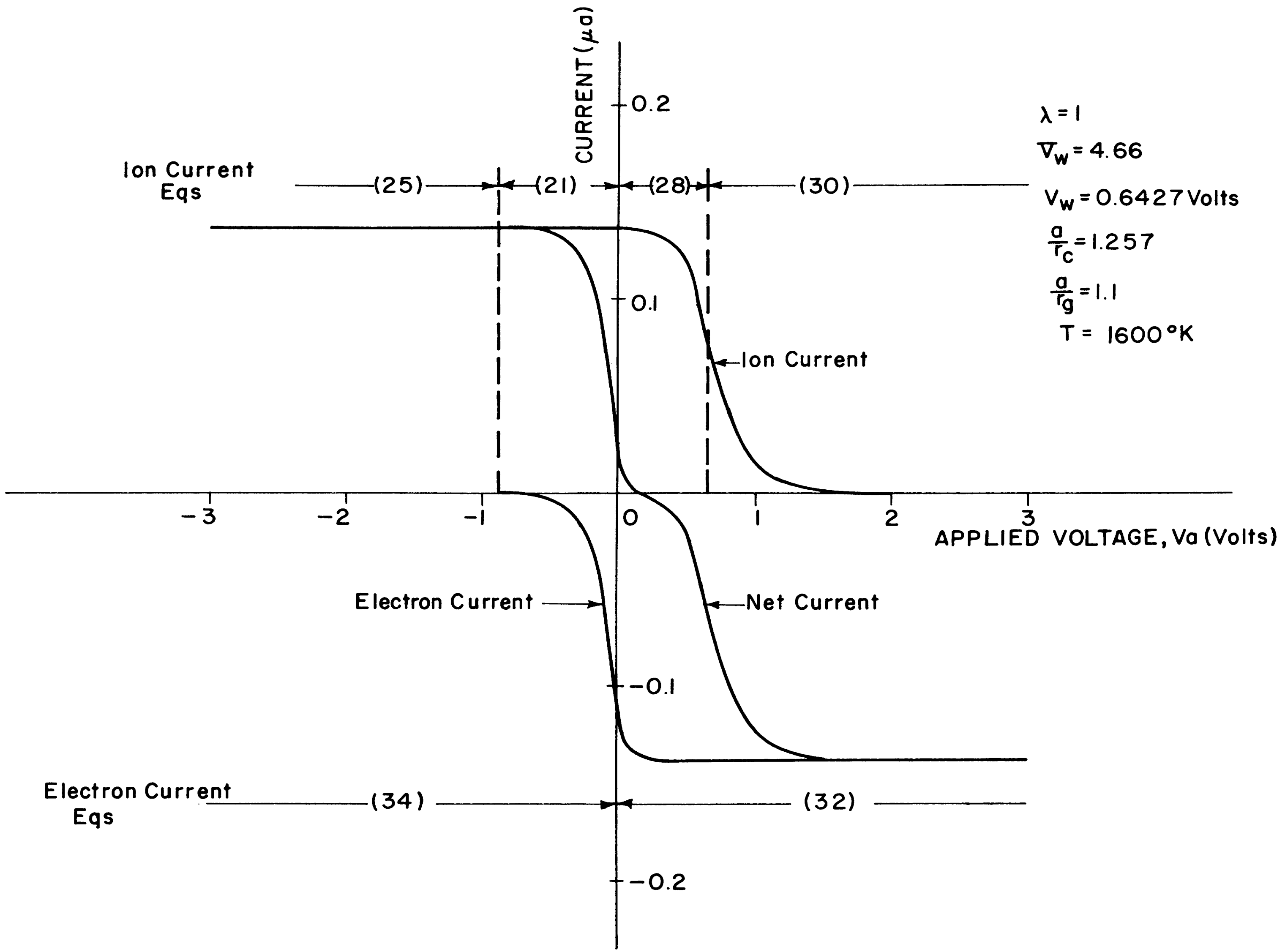

Fig. 23. A predicted volt-ampere characteristic of the 8-inch spherical ion trap which is moving at the most probable ion velocity (λ = 1).

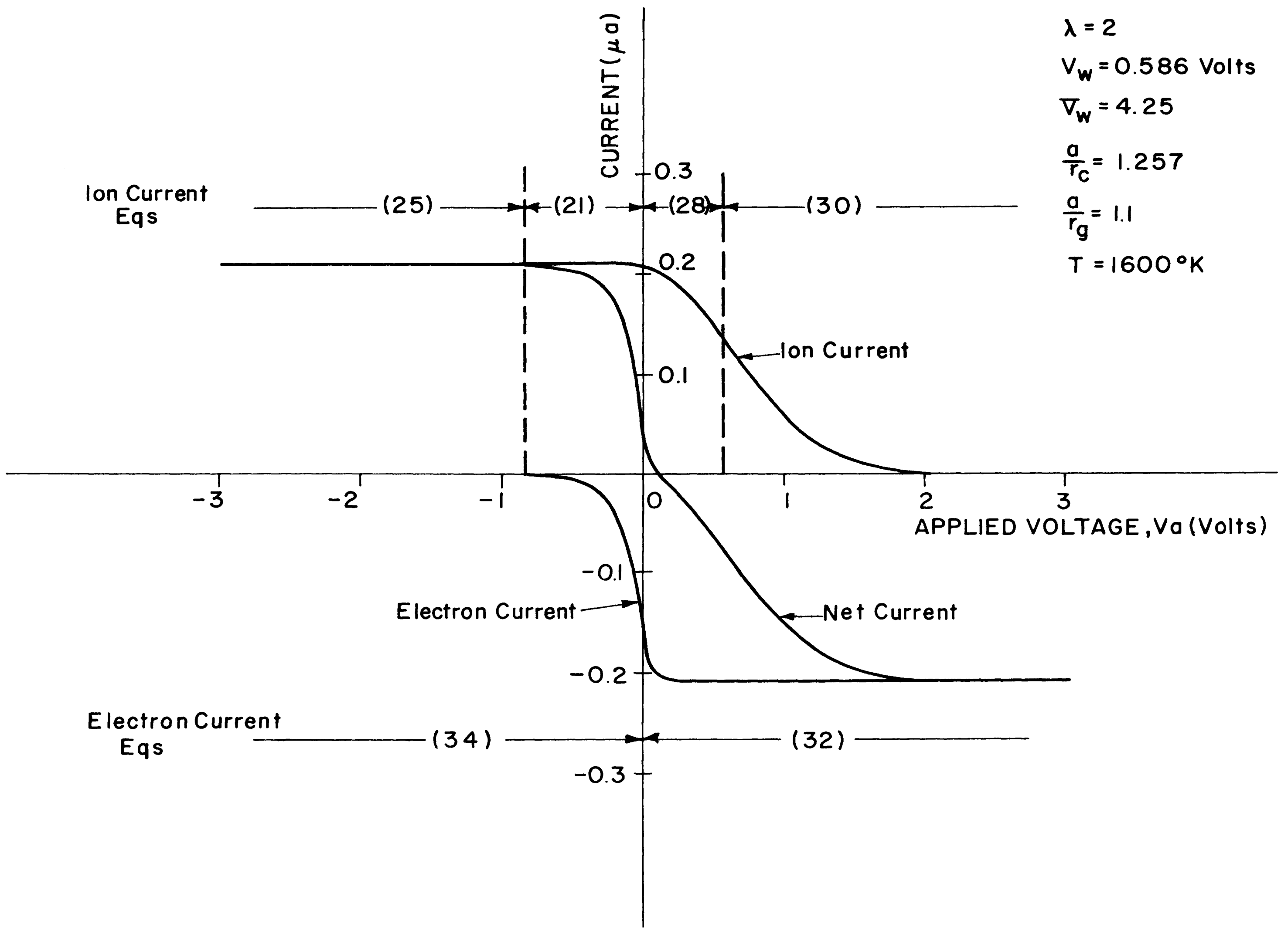

Fig. 24. A predicted volt-ampere characteristic of the 8-inch spherical ion trap which is moving at twice the most probable ion velocity ($\lambda = 2$).

and λ then should satisfy the implicit Eq. (39) for the chosen values of the other parameters. Since $\overline{V}_w$ represents the normalized equilibrium potential, we can easily determine the values of V_w because $\overline{V}_w = eV_w/kT$ as defined earlier. The corresponding values of the equilibrium potential V_w for T = 1600°K are 0.678V, 0.6427V, 0.586V, which are reasonable for the specified temperature. Using these values of V_w and Eq. (20a), we first compute the corresponding transition potentials which define the transition between ion current Eqs. (21) and (25).

$$\frac{V_a}{V_w} = \frac{\tau^2(\tan^2\phi - \gamma_o^2)}{\gamma_o^2(\tan^2\phi + \tau^2)} . \tag{20a}$$

Substituting the design parameters of the spherical ion trap, t = 0.04 in., d = 0.25 in., $r_c = 3.5$ in., $r_g = 4.0$ in., and the assumed sheath dimension $a/r_g = 1.1$, in (20a) we obtain,

$$\frac{V_a}{V_w} = 1.411. \tag{40}$$

To compute the voltage characteristics of the iron trap at the various velocity ratios, $\lambda = 0, 1, 2$, we solved (20a) for the corresponding transition voltages, $V_a = 1.411\ V_w$. Next, we used Eq. (25) for the ion current at applied voltages which are more negative than the transition value, and Eq. (21) for negative applied voltages of lesser magnitude. The electron current is given by (35) over the entire range of negative V_a.

For positive applied voltage, the ion current function (28) was used for V_a less than V_w and (30) for V_a greater than V_w, while the electron current is given by (33) over the entire range of positive V_a.

Discussion.—The resulting set of predicted volt-ampere characteristics of the ion trap are shown in Figs. 22, 23, and 24. Note that the *shape* of the current characteristic for negative V_a is dominated by the electron current which is exponential in nature. This region thus yields the *electron temperature* of the plasma. The *magnitude* of the current, however, is a function of the *ion density*. Conversely, the ion current dominates the shape of the positive V_a characteristic, and thus permits an interpretation in terms of *ion temperature*. Such interpretation is simple when the probe velocity is nearly zero, since the current changes nearly exponentially; however, at higher velocities the ion current behavior is more complicated hence necessitating a greater dependence upon the theory for the ion temperature determination.

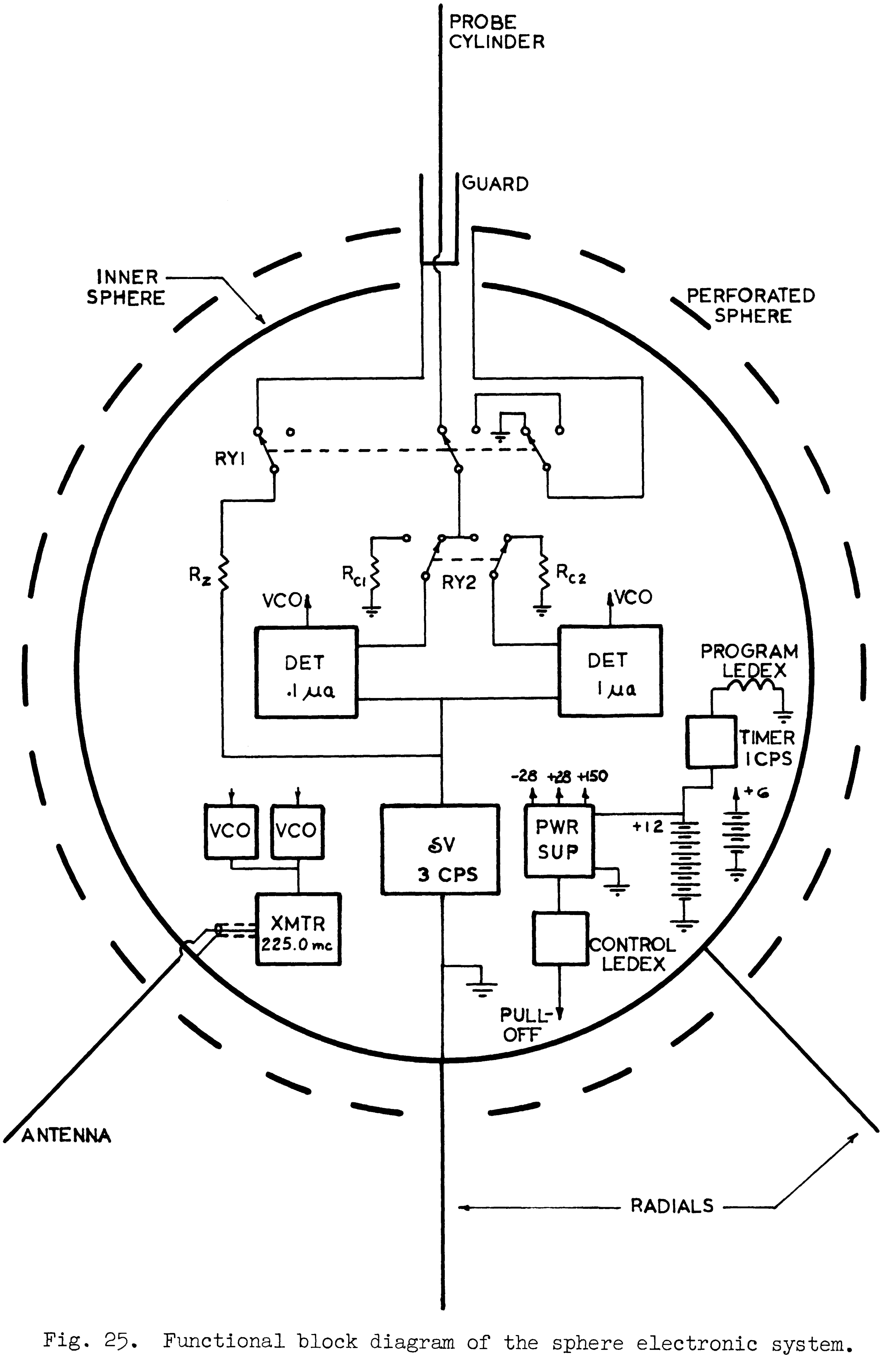

Fig. 25. Functional block diagram of the sphere electronic system.

3.0. IMPLEMENTATION OF THE ION TRAP—LANGMUIR PROBE EXPERIMENT

The design of an instrument capable of bridging the gap between the real world and the theories which attempt to describe certain aspects of the real world is a most challenging task. The theories of the previous sections predict wide variations in collected current in response to the changing ionospheric density experienced by the probe in passing through the E and F regions. Similarly, the wide variations in plasma temperature make necessary periodic changes in the magnitude of the voltage sweep applied to the collectors. The design is further complicated by the environmental factors of temperature, vibration and acceleration which are encountered in rocket borne measurements. The following sections contain a discussion of the 8-inch sphere design which has been evolved to mate the theory to the environment.

3.1. THE ELECTRONIC SYSTEM

3.1.1. General Description.—Figure 25 is a functional block diagram of the 8-inch sphere instrument shown in its Langmuir probe mode of operation. A sweep voltage, derived from the unit labelled δV, is applied through either a 0.1 microampere or a 1.0 microampere detector to the cylindrical collector. These detectors cover the expected range of currents of the two experiments throughout the ionosphere and are connected alternately to the appropriate collector. In-flight calibration of the system is achieved by connecting the resting detector to a known calibration resistor, R_c. Meanwhile the sweep voltage is also applied to the guard electrode through a compensation resistance, R_Z, whose value is selected to match the voltage drop across the detector input, which may be several millivolts. Thus the guard electrode voltage is made to closely follow the collector voltage. A simple electrometer voltmeter, not shown in the figure, is also included in the instrument to provide data for determining the accuracy of the guard-probe voltage match and to measure the equilibrium potential of the collector when the latter is allowed to float during the ion trap measurement. Note that, in the Langmuir probe mode, the perforated sphere is connected to the inner sphere and together they act as the plasma reference for the cylindrical probe.

The Ion Trap Mode of operation is achieved when relay RY1 is switched to its alternate position, which disconnects the perforated sphere from the inner sphere and inserts the current detector and voltage generator into the ion trap circuit.

3.1.2. δV Generator.—The δV generator produces the required sweep voltage by shaping the sawtooth output of a unijunction transistor relaxation oscillator. The schematic of the circuit, a photo of its printed circuit board, and a drawing of its output waveform are shown in Figs. 26, 27, and 28, respectively. The flat portion of the sweep is a zero reference voltage produced by the pair of diodes at the output of the generator. The output impedance of the generator is kept below 5k ohms to minimize the voltage drop due to the collected ionosphere currents. The sweep frequency is normally between 1 cps to 5 cps. This is normally a compromise between the ideal instantaneous sweep and the limitation introduced by the frequency response of the current detectors. The linearity of the voltage waveform is held to

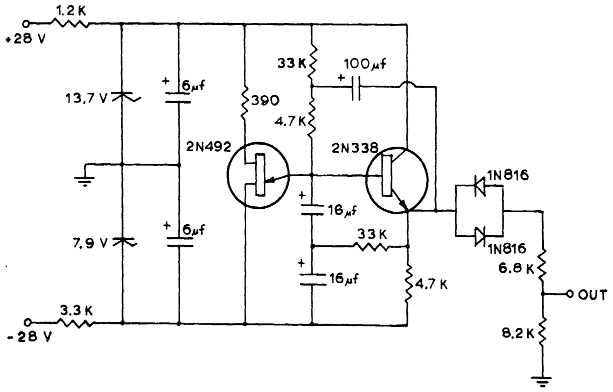

Fig. 26. δV generator schematic.

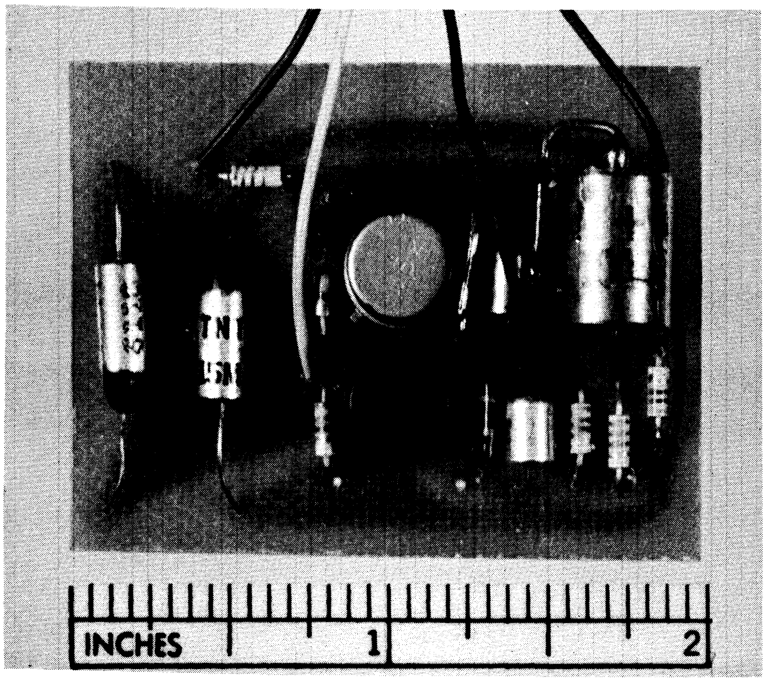

Fig. 27. δV generator circuit board.

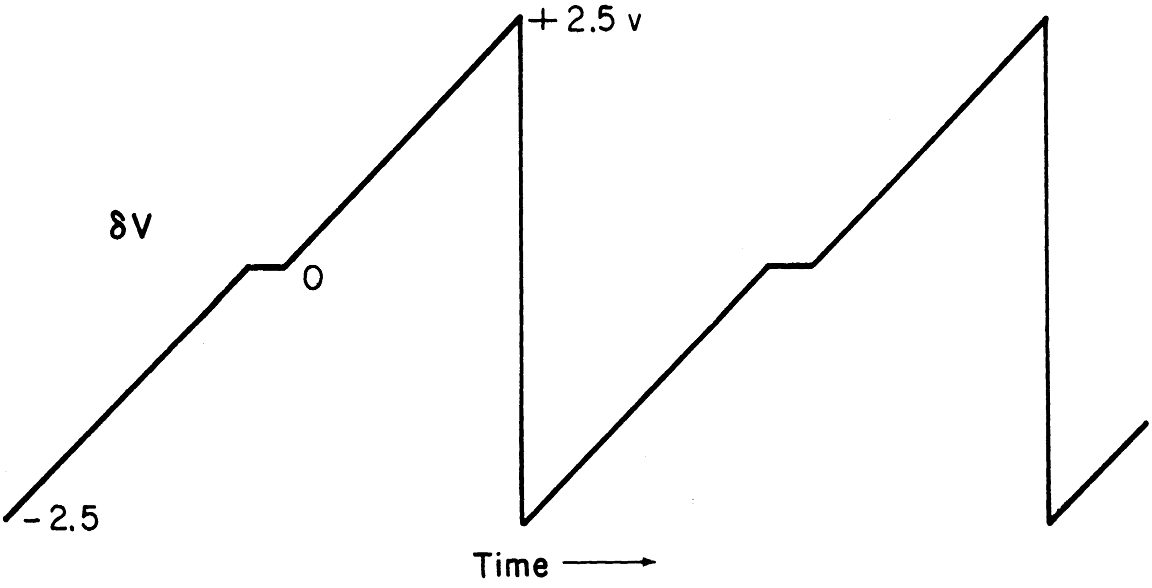

Fig. 28. δV output voltage waveform.

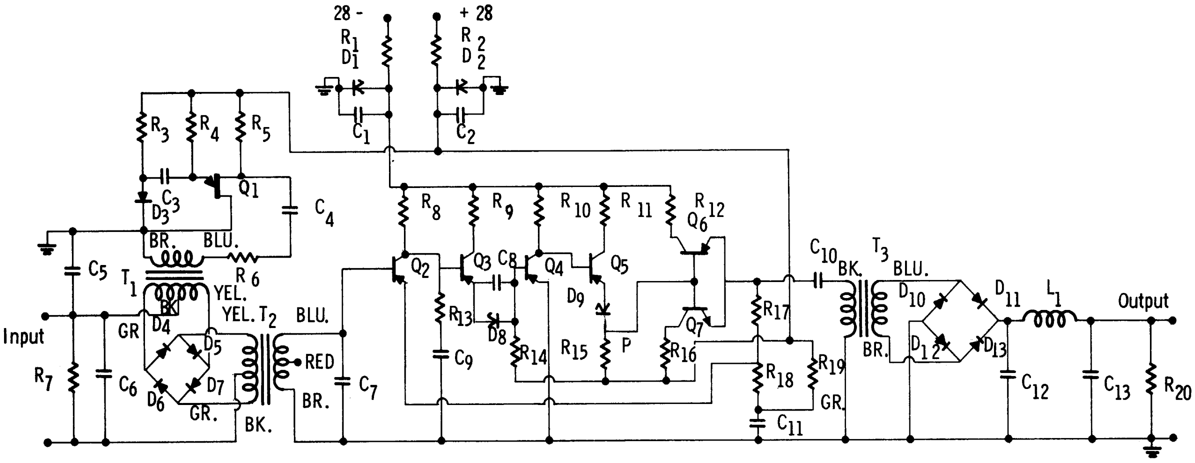

R_1 - 1 K
R_2 - 1 K
R_3 - 82 K
R_4 - 82 K
R_5 - 18 K
R_6 - 47 K
R_7 - 15 K
R_8 - 47 K

R_9 - 2.2 K
R_{10} - 47 K
R_{11} - 2.2 K
R_{12} - 2.2 K
R_{13} - 680 Ω
R_{14} - 47 K
R_{15} - 47 K
R_{16} - 2.2 K

R_{17} - 47 K
R_{18} - 100 Ω
R_{19} - 68 K
R_{20} - 10 K

C_1 - 8 μ f.
C_2 - 8 μ f

C_3 - .03μf
C_4 - .01μf
C_5 - 500μμf
C_6 - 500μμf
C_7 - .03μ f
C_8 - 12 μ f
C_9 - .005μf
C_{10} - .5 μ f
C_{11} - 6 μ f
C_{12} - .082 μ f

C_{13} - .082 μ f
D_1 - SV-24
D_2 - SV-24
D_3 - IN 98
D_4 - FD-300
D_5 - FD-300
D_6 - FD-300
D_7 - FD-300
D_8 - SV-11
D_9 - SV-5

D_{10} - IN 98
D_{11} - IN 98
D_{12} - IN 98
D_{13} - IN 98
L_1 - DI-T8
Q_1 - 2N492
Q_2 - CK67A
Q_3 - CK67A
Q_4 - CK67A
Q_5 - CK67A
Q_6 - CK67A

Q_7 - 2N213A

T_1 - DO-T24
T_2 - DO-T24
T_3 - DI-T22

Fig. 29. Schematic of the current detector.

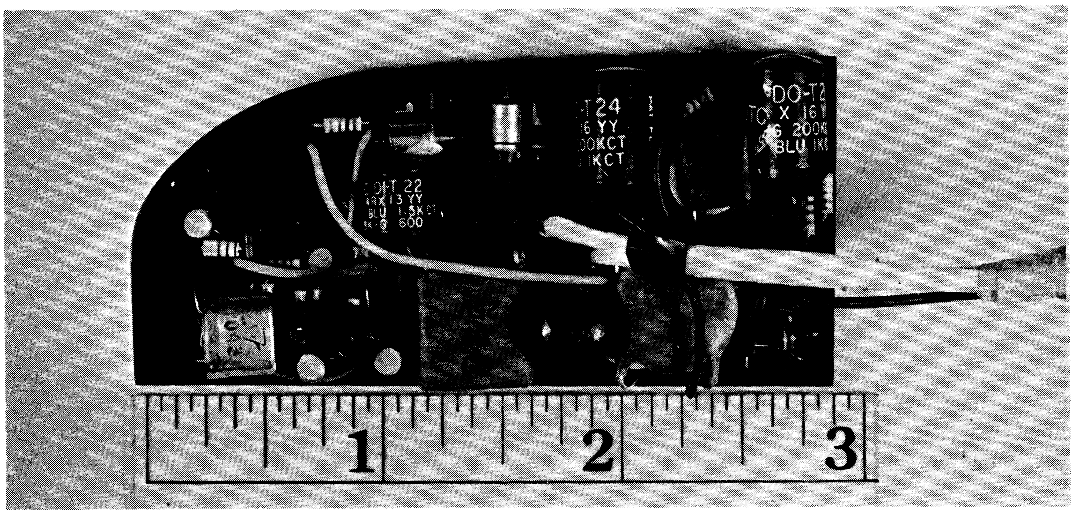

Fig. 30. Current detector circuit board.

within ±1% of the best straight line that may be superimposed on the sweep.

3.1.3. The Current Detectors.—A typical current detector, shown in schematic form in Fig. 29 and pictorially in Fig. 30, consists of a transistorized ring-bridge modulator, amplifier, and demodulator. The system was discussed in detail in earlier reports.[5,10] The maximum sensitivity presently obtainable with these units is a minimum detectable current of approximately 1×10^{-10} amperes. A typical curve of output voltage versus input current, shown in Fig. 31, indicates that the detector responds identically to both positive and negative input currents. The linearity of the input-output characteristic is normally better than 1% except in the null area near zero output. When linearity in the zero current portions of the probe current characteristic is deemed important, the detectors are current biased so that the null output occurs at some value of input current other than zero. The input impedance of the detector depends on its sensitivity but is normally maintained below 10% of the minimum impedance represented by the ionosphere. This tends to minimize corrections that must be made when a significant portion of the applied voltage is dropped across the detectors. A typical input impedance of a 1 microampere detector is approximately 10k ohms. The frequency response of the detectors is measured in terms of the rise and fall times between 10% and 90% of full scale output when a full scale current step is applied at the input. The response time is maintained better than 5 milliseconds; a sufficiently fast response for the voltage sweep period of 200 to 1000 milliseconds.

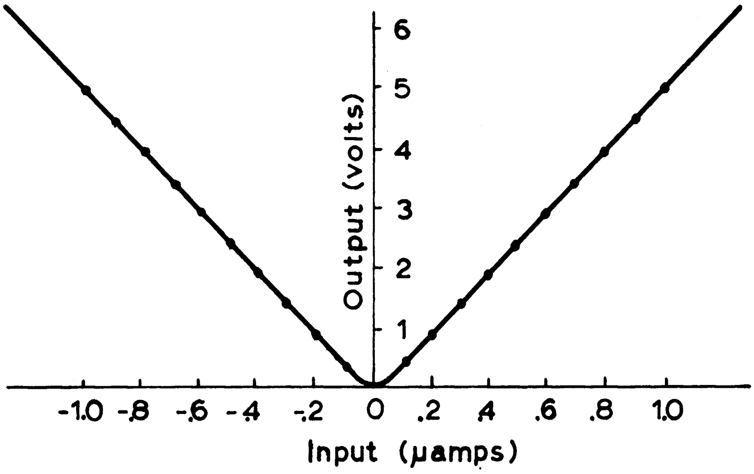

Fig. 31. Input-output characteristic of a typical 1 μamp detector.

Some interesting problems arise in the use of these detectors. The leakage resistance from the input leads to ground must be very high in this application since the resulting leakage current adds algebraically to the collected ionosphere currents. The input leads from the probe or ion trap must contain rf filtering as they are part of the antenna system, and, at the same time, capacitance from the input leads to ground must be kept below about 200 picofarads so as not to limit the frequency response of the detectors. If the detectors are to be used in series, the frequencies of the detector drivers must either be synchronized or be kept far enough apart so that beat frequencies which may develop are high enough to be filtered efficiently. Similarly, the detector driver frequencies must either be kept away from the power supply ripple frequency or synchronized to it if interference problems are to be avoided.

3.1.4. Control and Timing Circuits.—Relays are used to perform all functional switching, as they may be placed in convenient locations to keep sensitive lead lengths to a minimum. The relay coils are energized at the desired times by the Program Ledex, which in turn is stepped by a transistorized pulse generator once every second. The power supply is energized by the Control Ledex, which is activated through umbilical cables from the block house.

3.1.5. Power Supply.—Primary power is furnished by two sets of Yardney HR-1 Silver Cells. One, a 6-volt pack, is used to power the telemetry transmitter filaments and to provide Ledex position indication to the block house. The second pack, 12 volts, is used in the primary of a d-c—d-c converter which furnishes regulated plus and minus 28 volts to the instrument circuitry and 180 volts to the transmitter. The converter is shown in Figs. 32 and 33.

Heat sinking the converter transistors presents a potential problem because approximately 35 watts is dissipated within the sphere, little of which can be radiated by the polished stainless steel skin. However, with a conservatively designed power supply, no special precautions are required; the transistors are simply placed in blocks of aluminum, and tests have shown that the supply will not overheat during flight times of less than 15 minutes.

3.1.6. Telemetry.—The transmitter used is a Bendix TXV-13, 2 watt, PM-FM unit, and the voltage controlled oscillators, each having a volume of 1.4 cubic inches and a weight of 2 ounces, are Vector TS-54 units which accept a 0-5 volt input and deviate ±7.5% of center frequency. Transmitter rf output is coupled through a 50 ohm coaxial cable to a 1/4 wave ground plane antenna formed by a 12-inch whip, three radials, and the 8-inch sphere itself.

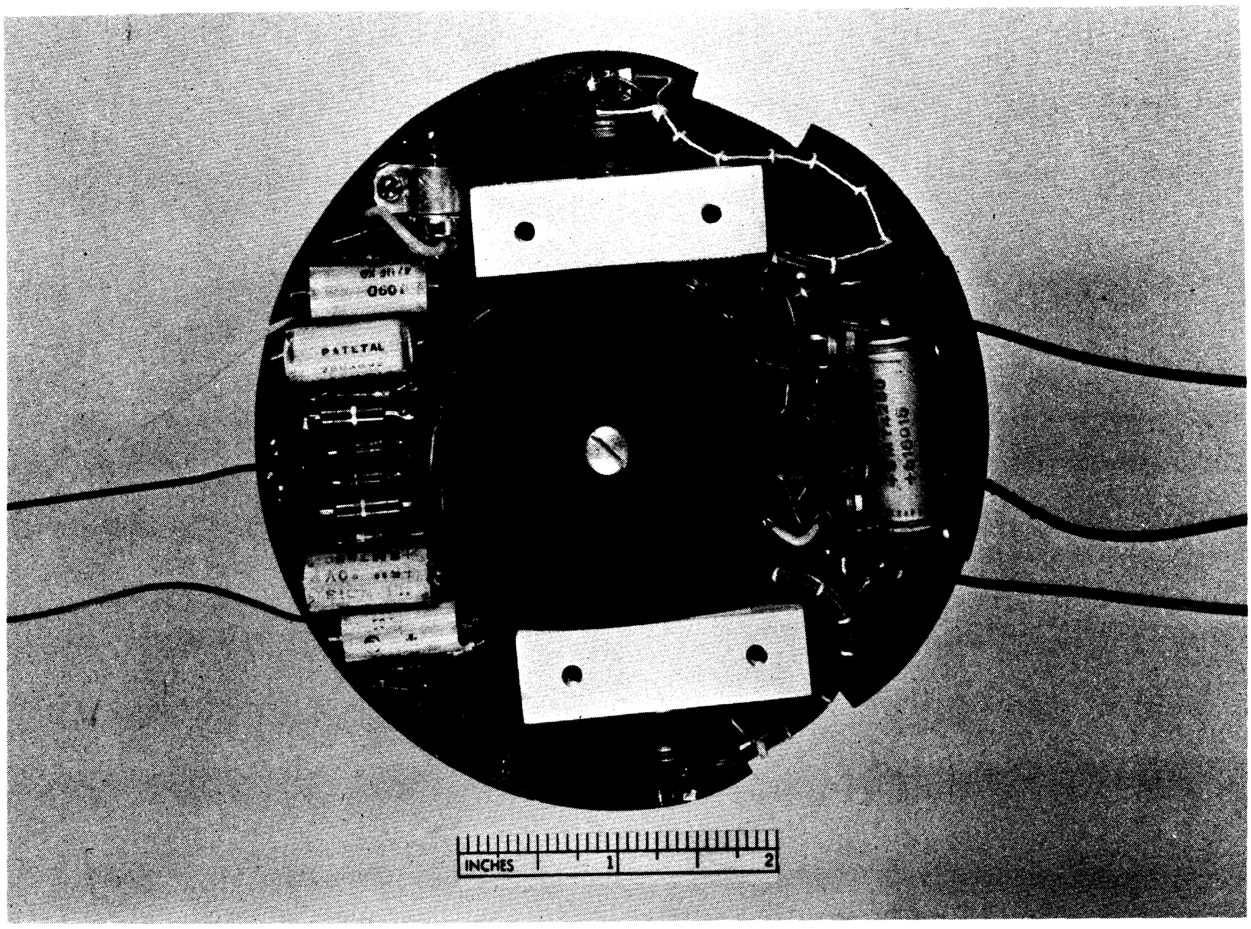

Fig. 32. d-c—d-c converter circuit board.

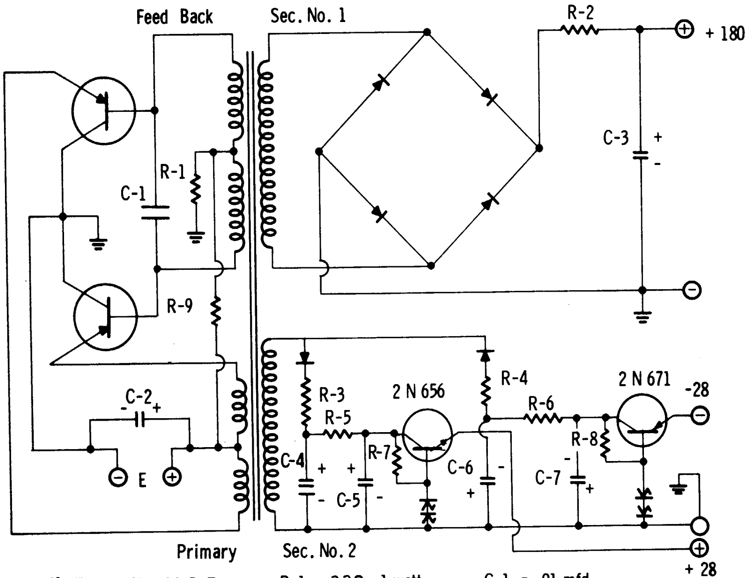

PR. 41 Turns No. 18 C.T.
F.B. 70 " No. 30 C.T.
S No. 1 355" No. 27
S No. 2 85 " No. 30
PWR. TRAN. 2 N540A
RECT. HD-6754

R-1 = 330 1 watt
R-2 = 39 Ω 1/2 w
R-3 & 4 = 10 "
R-5 & 6 = 100 "
R-7 = 4.7 k 1/10 w
R-8 = 8.2 k 1/10 w
R-9 = Same as R-1

C-1 = .01 mfd
C-2 = 47 mfd 50 v
C-3 = 4 " 250 v
C-4 & 6 = 5 " 50 v
C-5 & 7 = 47 " 50 v

E - Input = 11.5 v
I - Input = 2.5 amps

Fig. 33. d-c—d-c converter circuit board schematic.

3.1.7. In-Flight Calibration.—In-flight calibration of the current detection system is accomplished by the substitution of a known resistor for the "ionosphere" periodically throughout the flight. Referring to Fig. 25, the calibrate resistors, R_{c1} and R_{c2}, are chosen to provide full-scale input current to the current detectors. Before flight, the calibrate resistances and the δV generator output are accurately measured.

3.1.8. Accuracy.—The current measurement accuracy of the experiment is determined by the accuracy to which the δV voltage and the calibrate resistance (R_{c1} or R_{c2}) is known. It would seem that any current detector nonlinearity would also be an important contributor to the maximum error allowed for the experiment. However, a comparison of the δV waveform before flight with an "in-flight" calibration record enables the magnitude of any detector nonlinearity to be determined. This error can then be corrected during the data reduction to hold the linearity within the limits specified for the δV.

The internal impedances of the δV generator and current detectors are another source of error. For example, should the effective impedance of the ionosphere at some instant equal the output impedance of the δV plus the input impedance of the current detector, the voltage at the probe would become exactly half the no-load δV voltage. In this case, a measurement of the circuit impedance before flight enables the δV voltage at the probe to be corrected during the data reduction. Normally, the internal impedance is smaller than the effective impedance of the ionosphere by an order of magnitude or more.

The peak δV voltage is held within ±1% of the peak voltage measured at

75°F, over a temperature range from 50°F to 100°F. The linearity of the δV is also held within ±1% of the "best straight line" at 75°F, for the same temperature range. The calibrate resistors are measured to within 0.5%, and low temperature coefficient resistors are used. The maximum error in the current measurement thus can be held to less than 2.5%.

3.2. MECHANICAL DESIGN OF 8-INCH SPHERE

This section describes the construction of the major parts of the sphere and placement of components within the sphere.

3.2.1. General Description.—The sphere is shown in Fig. 34 with the upper half of the perforated skin removed to expose the inner sphere. There are four nylon insulators projecting from the bottom half of the inner sphere, in addition to the one projecting from the top of the sphere, whose purpose is to provide about 1/2 inch spacing between the inner and outer spheres. The four wires extending from the sphere terminate at coaxial connectors in the center of the nylon insulators; the topmost wire serves as the Langmuir probe and as a radial of the antenna ground plane, the left wire is the antenna, and the remaining two are radials of the ground plane. The control plug, not visible, is in a fifth nylon insulator directly beneath the sphere.

The sphere surfaces, antenna, radials, probe, and all assembly screws exposed to the ionosphere are stainless steel to provide a constant contact potential throughout, and because stainless steel has a high work function which helps to minimize photo-electric effects. In addition, stainless steel offers ease of maintenance of clean collector surfaces.

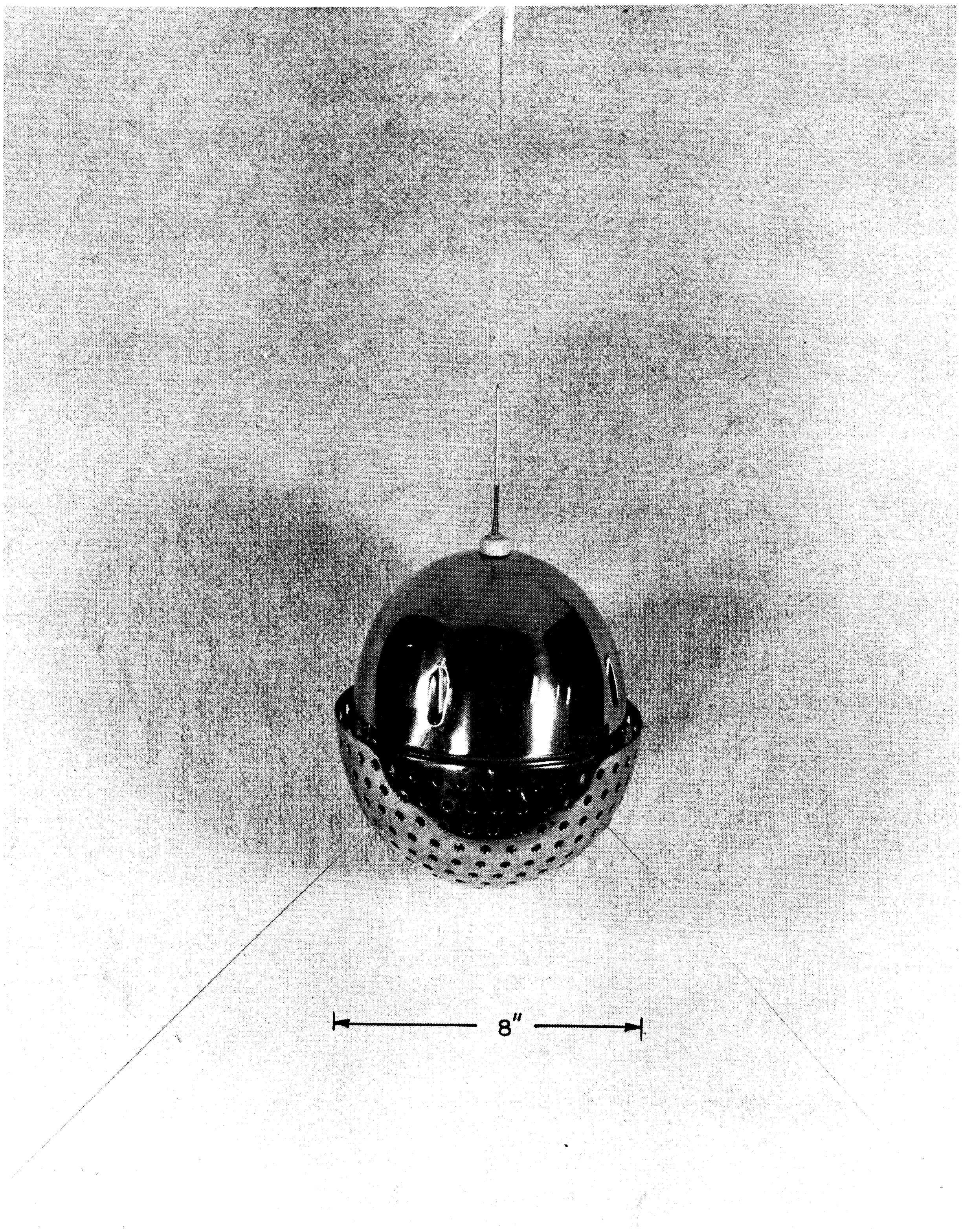

Fig. 34. Sphere with upper half of perforated skin removed.

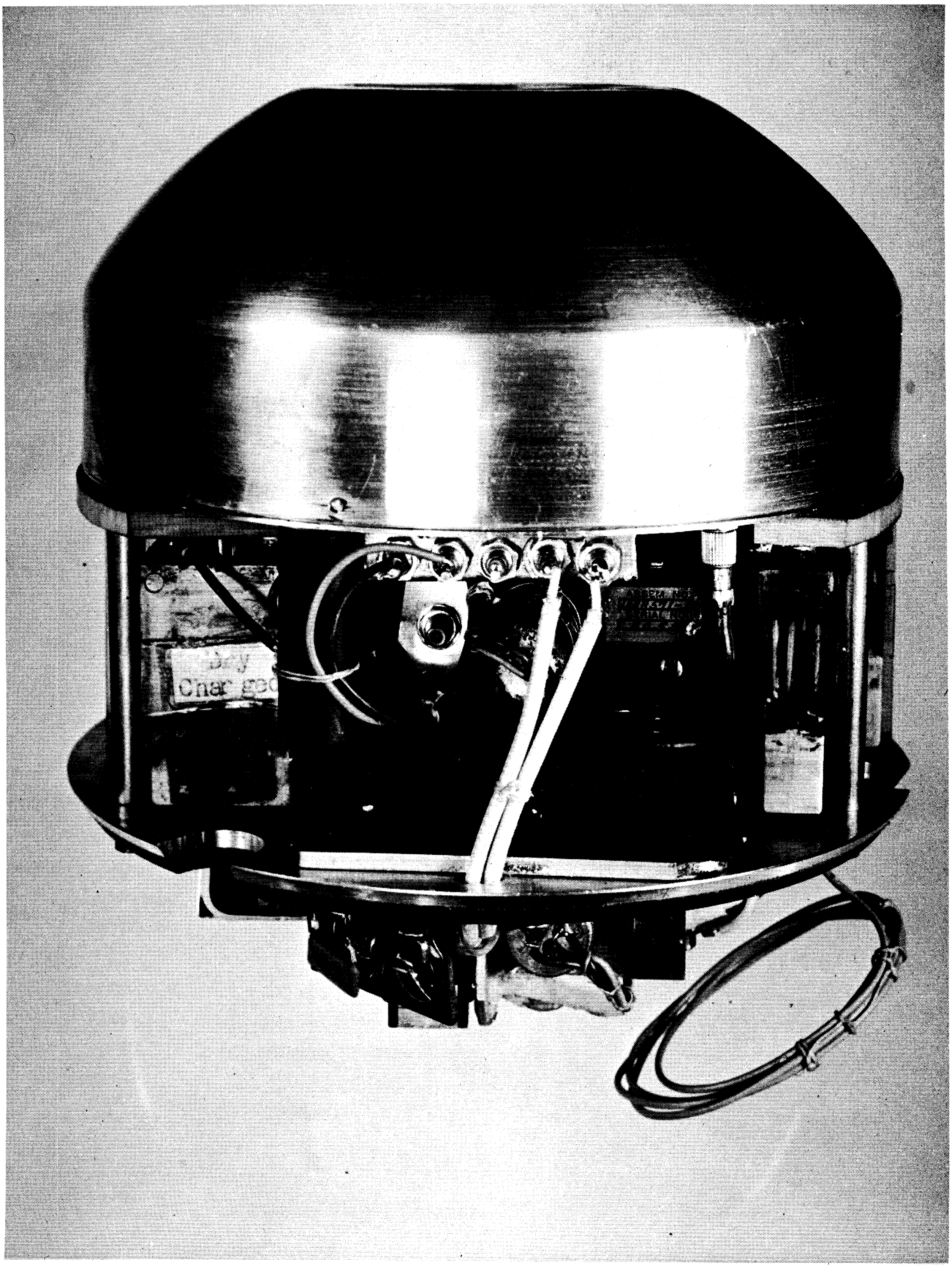

Fig. 35. Electronics package.

Figure 35 exposes the instrument package as assembled within the sphere. The plug-in can on the upper deck contains the current detectors, δV generator, VCO's, program Ledex, relays, and associated wiring. Beneath this can is the transmitter, and below the lower deck is the d-c—d-c converter. The HR-1 batteries may be seen on each side of the transmitter; the control Ledex is not visible. Just beneath the upper deck, partly visible, in the center of the figure is a small can containing rf filtering for each lead entering the plug-in instrument can. Plastic foam is used to secure all wiring from possible breakage caused by vibration and acceleration.

3.2.2. Perforated Sphere (The Grid).—The perforated sphere is approximately 8 inches in diameter and, in conjunction with the inner sphere, forms the ion trap. There are over 500 holes in this surface, each hole being 1/4 inch in diameter. These holes are as evenly spaced as is practicable to present a uniform hole area to the ionosphere, regardless of sphere orientation. To facilitate assembly and disassembly, the perforated sphere is split into hemispheres.

3.2.3. Inner Sphere.—This sphere is about 7 inches in diameter and is also split, as shown in Fig. 36, to facilitate assembly. The oval-shaped grooves that may be seen in the top hemisphere provide access for screws which hold the two halves together. Although the two hemispheres make a good electrical contact where they press together at the rims, the screws also insure that the sphere is, electrically, one surface. The "O"-ring, shown with the hemispheres, fits into a groove in the lower hemisphere rim and provides a seal so that the sphere may be pressurized. The screws holding the sphere

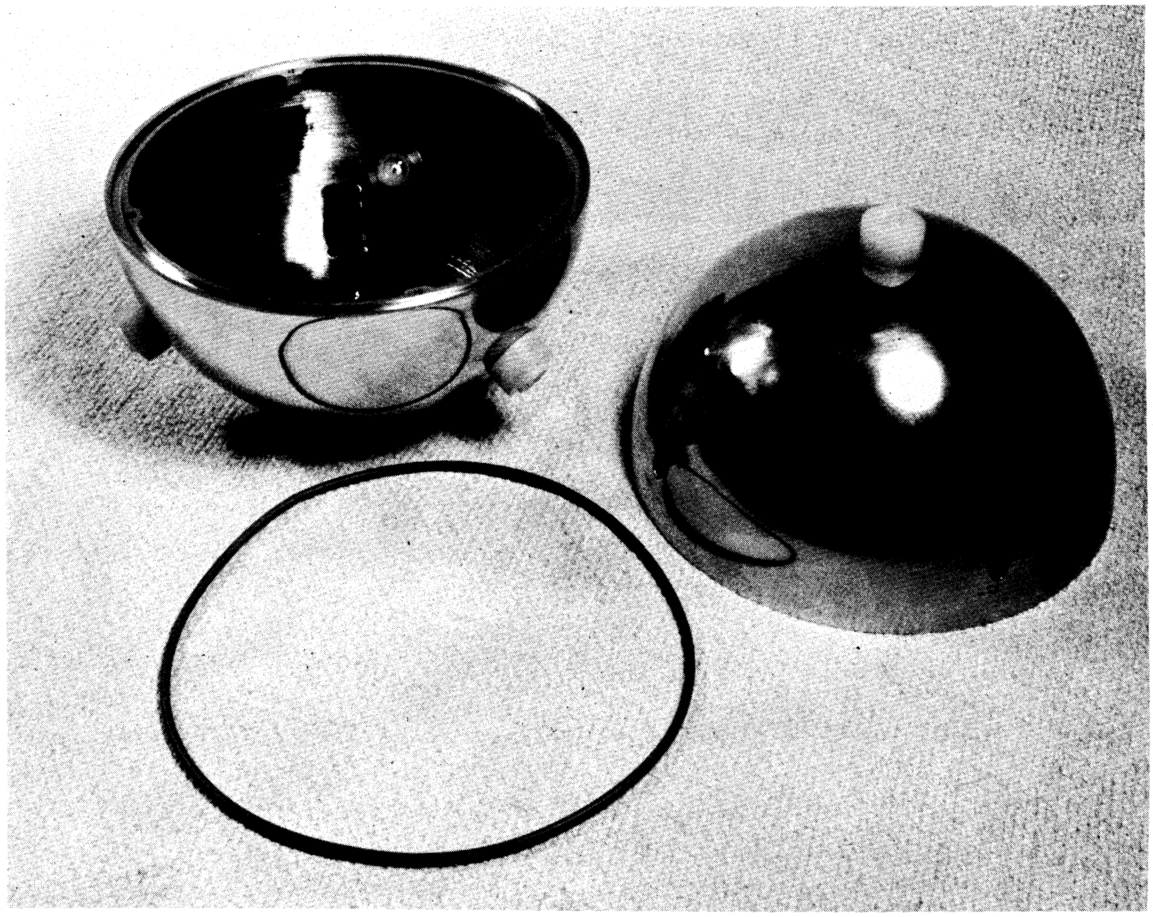

Fig. 36. Inner sphere.

together also have seals under their heads, but they are so constructed that the screw heads continue to make a good electrical contact to the upper hemisphere. The nylon insulators screw into the sphere and are threaded with a standard pipe thread to increase the tightness of the fit. In addition, the threads of both the insulators and the coaxial connectors within the insulators are coated with a bonding agent to insure that a good pressure seal is maintained.

Inside the bottom hemisphere may be seen one of three supports which are welded to the skin. These supports are drilled and tapped to provide a mount for the instrument package.

3.2.4. Probe, Antenna and Radials.—The probe, antenna and radials are shown in Fig. 37. The probe is the most complex of these pieces, being comprised of a spring, guard and probe cylinder. The spring makes the probe flexible and thereby minimizes the chance of probe damage during ejection of the sphere from the nose cone. The guard, which is soldered to the spring, is a hollow tube. A flexible wire within the spring connects the probe cylinder to the inner conductor of the coaxial connector. The probe cylinder is inserted within the guard and insulated from it by a length of teflon spaghetti. The probe cylinder is a piece of stainless steel piano wire, .023 inch diameter, which protrudes 7 inches beyond the guard. The total length of the assembled piece is about 10 inches; the area of the probe cylinder surface is .50 square inches, as compared to the guard surface, which is .73 square inches.

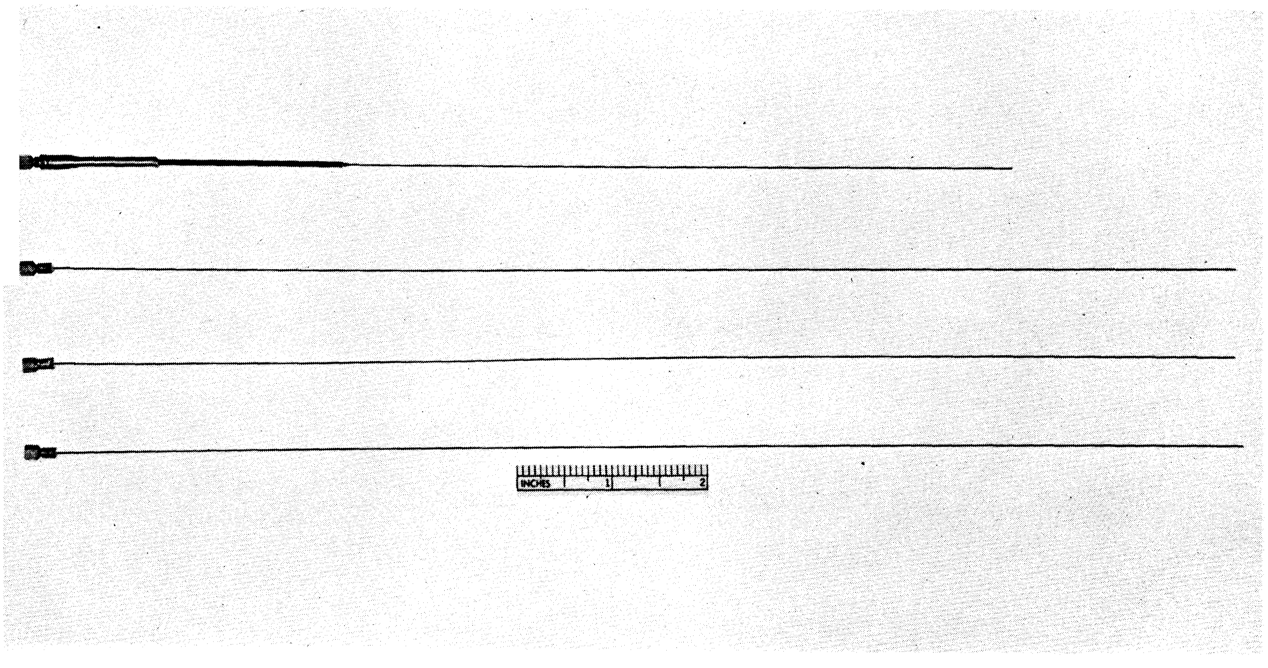

Fig. 37. Probe, antenna, and radials.

The antenna and ground plane radials are identical except that the radials are grounded to the sphere, and the antenna is insulated and connected to the transmitter rf output. Stainless steel piano wire is also used for these pieces, but no spring is inserted at the base, as the wires themselves act as nearly indestructable springs. (A spring is especially undesirable in the base of the antenna because it acts as an unneeded base loading coil in the rf circuit). Each wire is soldered to a coaxial connector and cut to a quarter wavelength of the telemetry frequency, typically 225.0 mcs.

3.2.5. Decks and Enclosure.—Figure 38 displays the two aluminum decks and spun aluminum cover which support and contain the instrumentation. The deck on the left mounts on the supports in the bottom hemisphere described previously, and below it, in what becomes a shielded compartment, is mounted the d-c—d-c converter. This deck acts as the transmitter and converter heat

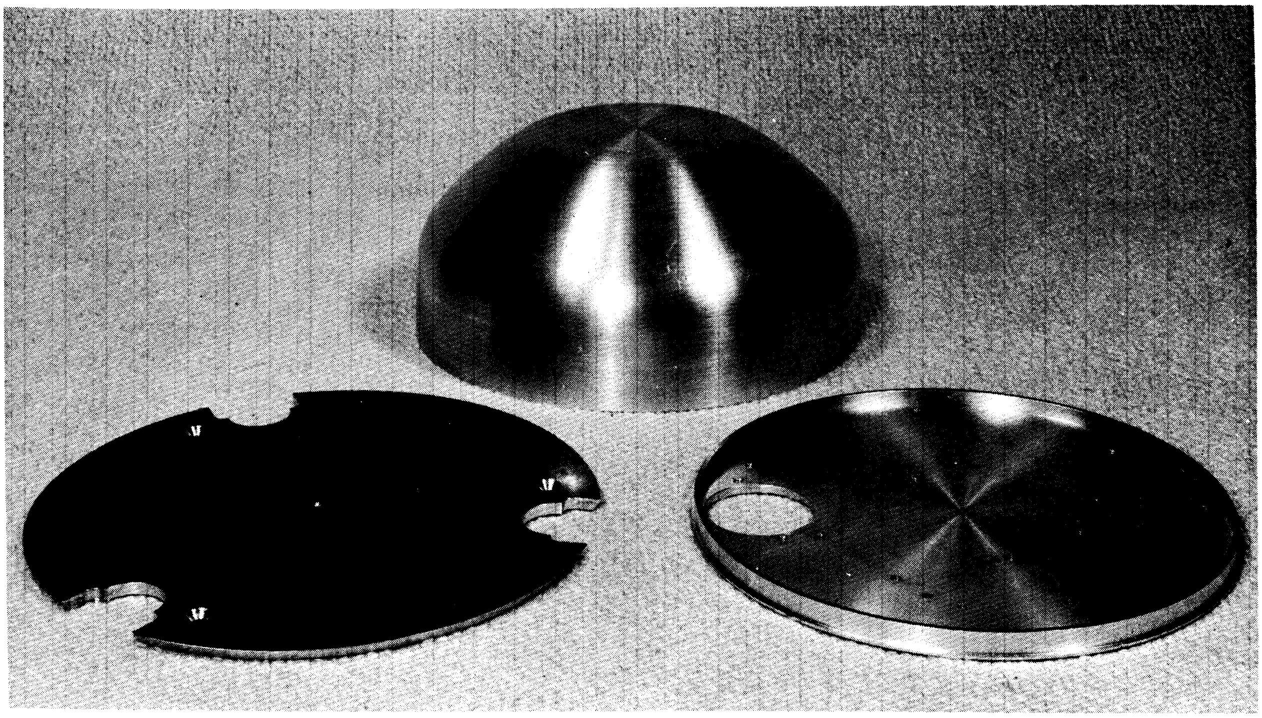

Fig. 38. Decks and instrumentation enclosure.

sink; thus, to aid in conduction of heat to the skin, its edges are beveled to permit maximum contact with the bottom hemisphere.

The deck on the right in conjunction with the can which fits onto it, supports and shields the current detectors, δV generator, voltage controlled oscillators, program Ledex, and associated wiring. A view of these components as they are mounted on the deck (unwired) is shown in Fig. 39. The Ledex pulsing generator and rf filters are mounted beneath the deck.

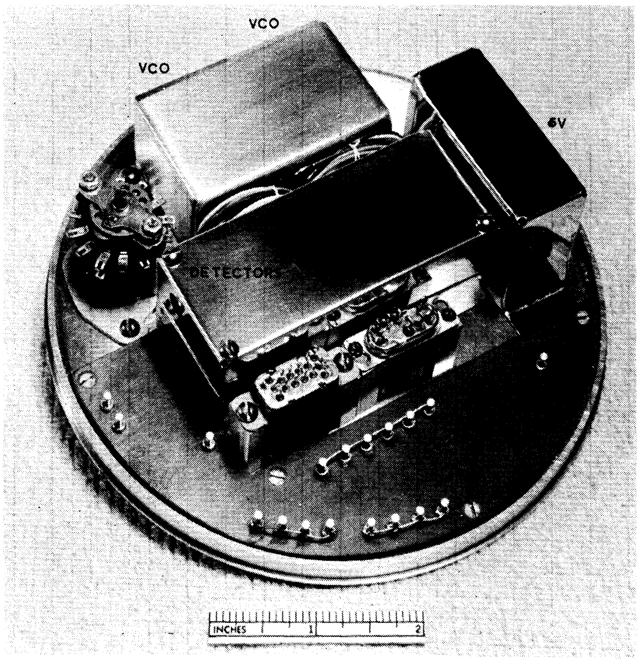

Fig. 39. Unwired instrument deck.

3.3. THE NOSE CONE AND SPHERE EJECTION SYSTEM

3.3.1. Introduction.—This section describes the design and construction of the clamshell nose cone which shields the 8-inch sphere throughout the launch phase and, at a predetermined time, separates it from the vehicle. Several difficult problems arise in the design of an ejection-type nose cone. The two most significant of these arise from aerodynamic forces and the aerodynamic heating and their ultimate effect upon the proper functioning of the system. The dominant design philosophy has been to minimize the number of critical functions necessary for ejection and to make each function as positive and fail-safe as possible. Because of this, a pyrotechnic release system with four-fold backup and a relatively non-critical clamshell opening action was selected. The latter allows for large thermal expansions and relatively loose mechanical tolerances. A similar system has been used with the Dumbbell technique.[5]

3.3.2. The Mechanical Design.—Figure 40 shows the nose cone as it appears just before the ejection of the sphere which occurs when the opening angle reaches 60° and the spring-loaded plunger is released. In this photo, the plunger had not been depressed and latched so that the sphere could be seen better.

The clamshell-type nose cone halves which provide the required aerodynamic shape during the early phase of the flight are hinged to the cylindrical aluminum casting and are geared to open together. The sphere rests on the plunger which is latched down mechanically until the nose cone has opened sufficiently to permit the sphere to clear all obstructions upon ejec-

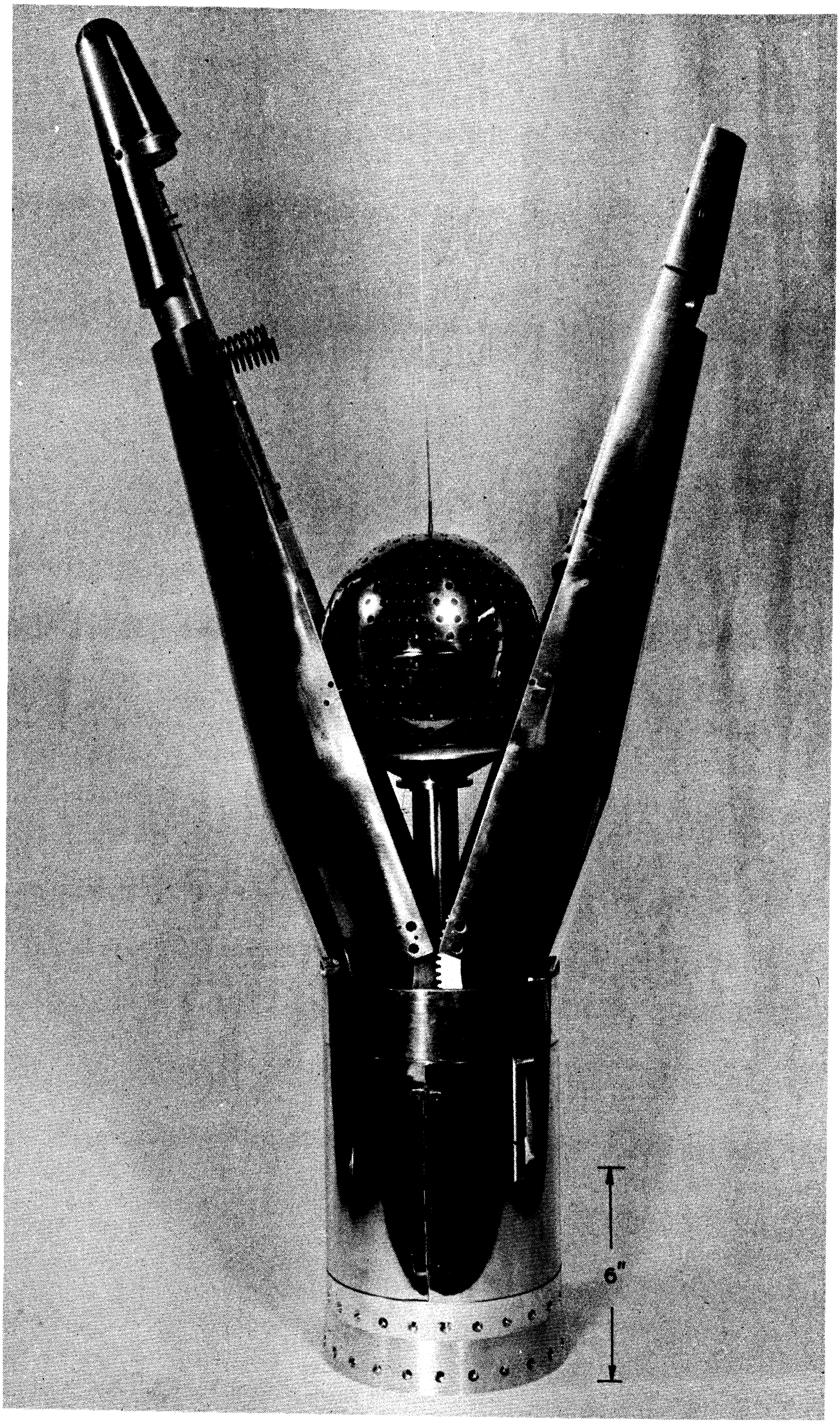

Fig. 40. Nose cone and sphere.

tion. A magnesium frangible ring holds the nose cone closed against the force of two springs. A "g"-actuated mechanical timer, which is released by the sustained thrust of the launch, initiates the ejection sequence at a prescribed time when the drag forces should have fallen well below the ejection forces. The timer provides a switch closure which carries current from a set of wet cells through four parallel-connected explosive squibs mounted under the frangible ring which when shattered permits nose cone opening, release of the plunger, and ejection of the instrument.

The forward section of the enclosure consists of two split halves which are machined from aluminum castings and a solid stainless steel tip. These are shown disassembled in Fig. 41. The flat interfaces are machined first so that the halves may be held together for subsequent machining. A recessed channel is machined around the nose cone to provide for flush mounting of the magnesium frangible ring. Four cylindrical pockets equally spaced around the channel are provided to mount the squibs and their thermal insulators which prevent premature detonation due to aerodynamic heating. The frangible ring is made in two parts which are fastened together with four recessed socket head cap screws at the split. The ring is relieved slightly above each of the four squibs to control the fracture line. The ring, a squib, a lamicoid insulator, and another view of a cone half are shown in Fig. 42.

Two 35-lb springs, used to provide opening force, are mounted just below the nose tip, as can be seen in Fig. 40. Steel dowels, mounted on one half of the nose, mate to holes in the opposite half and provide positive alignment and elimination of shear strain on the frangible ring.

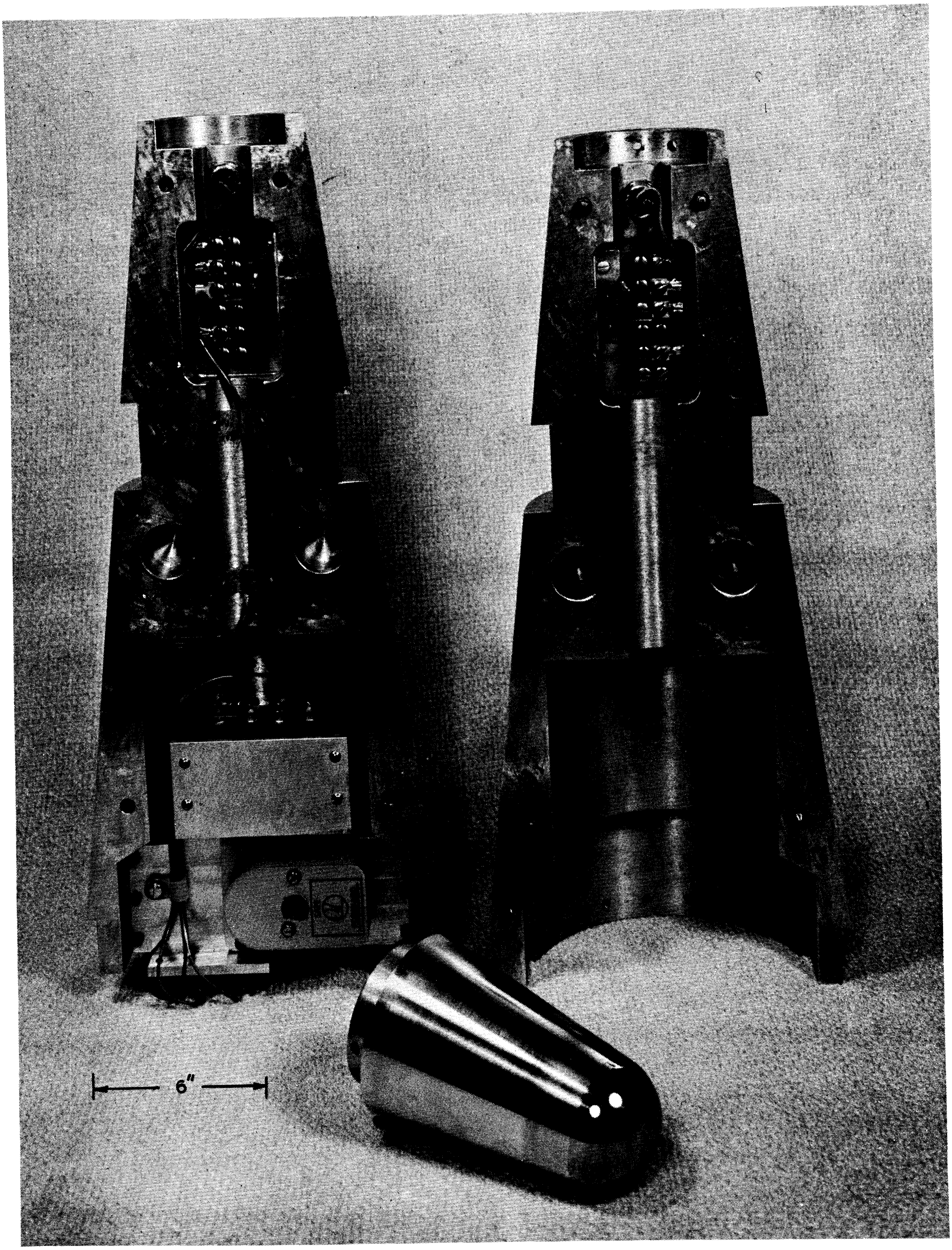

Fig. 41. Nose tip and upper portion of nose cone disassembled.

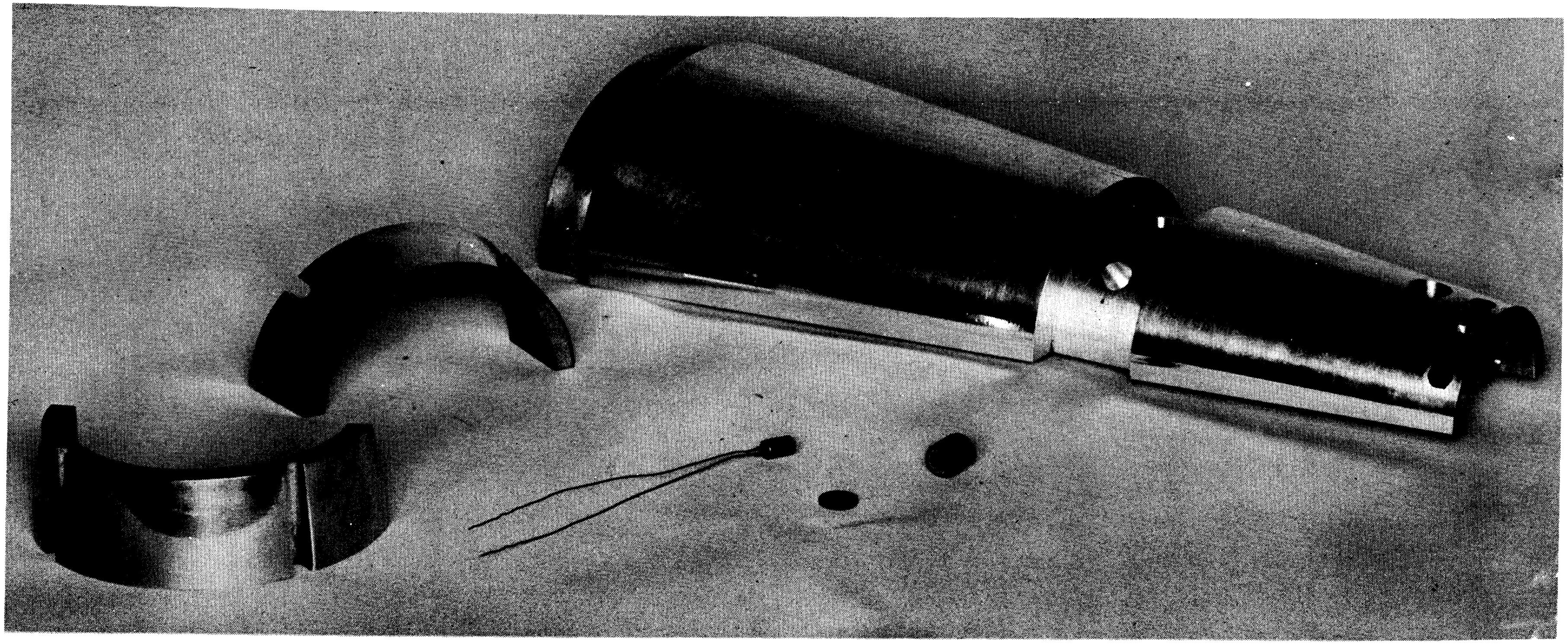

Fig. 42. Cone half with squib insulator assembly and frangible ring.

In the lower portion of the cone section, space and mounting faces for electrical components of the system are provided. A 6-volt HR-1 battery pack which provides the squib current and the "g" actuated mechanical timer may be seen mounted in Fig. 41.

At the base of the jaws, split gear segments are mounted on one side to force the jaws to open together, and on the other side, a spring-loaded piston is mounted to aid in forcing the jaws to the full open position and then to lock them open. These devices are shown in Fig. 43, which is a view looking into the nose cone with the plunger removed.

The plunger latch mechanism can also be seen in this view. The plunger is held in the depressed position by this strong latch pressing against a machined shoulder on the plunger assembly. When the nose cone is closed, the latch is held positively in position to prevent premature release due to vibration or radial accelerations. The linkage is so arranged that the latch does not move until the jaws are open approximately 60°, and then it quickly unlatches, providing a positive release when the jaws are sufficiently open to clear the ejecting sphere.

A view of the lower part of the nose cone with the plunger installed, but not depressed and latched, is shown in Fig. 44. The skin has been removed to show the spring and plunger. The plunger guide which is bolted to the floor of the compartment fits within the hollow plunger shaft, providing a bearing to guide the plunger when it is depressed or released. In addition, the guide supports the spring as it is compressed (to about 60 lb) and retains the plunger at the end of its travel during ejection. Space is also

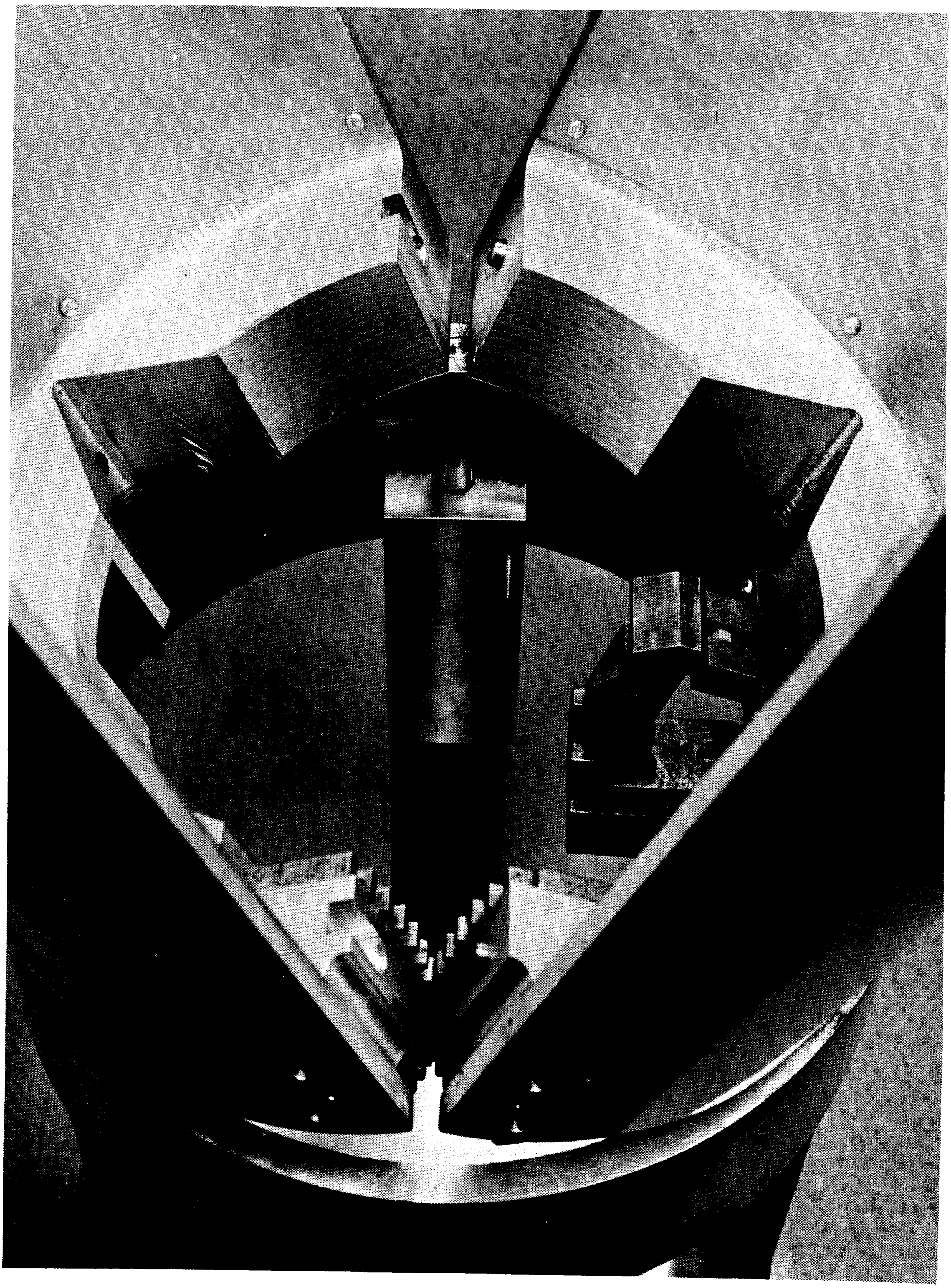

Fig. 43. Open nose cone with plunger removed.

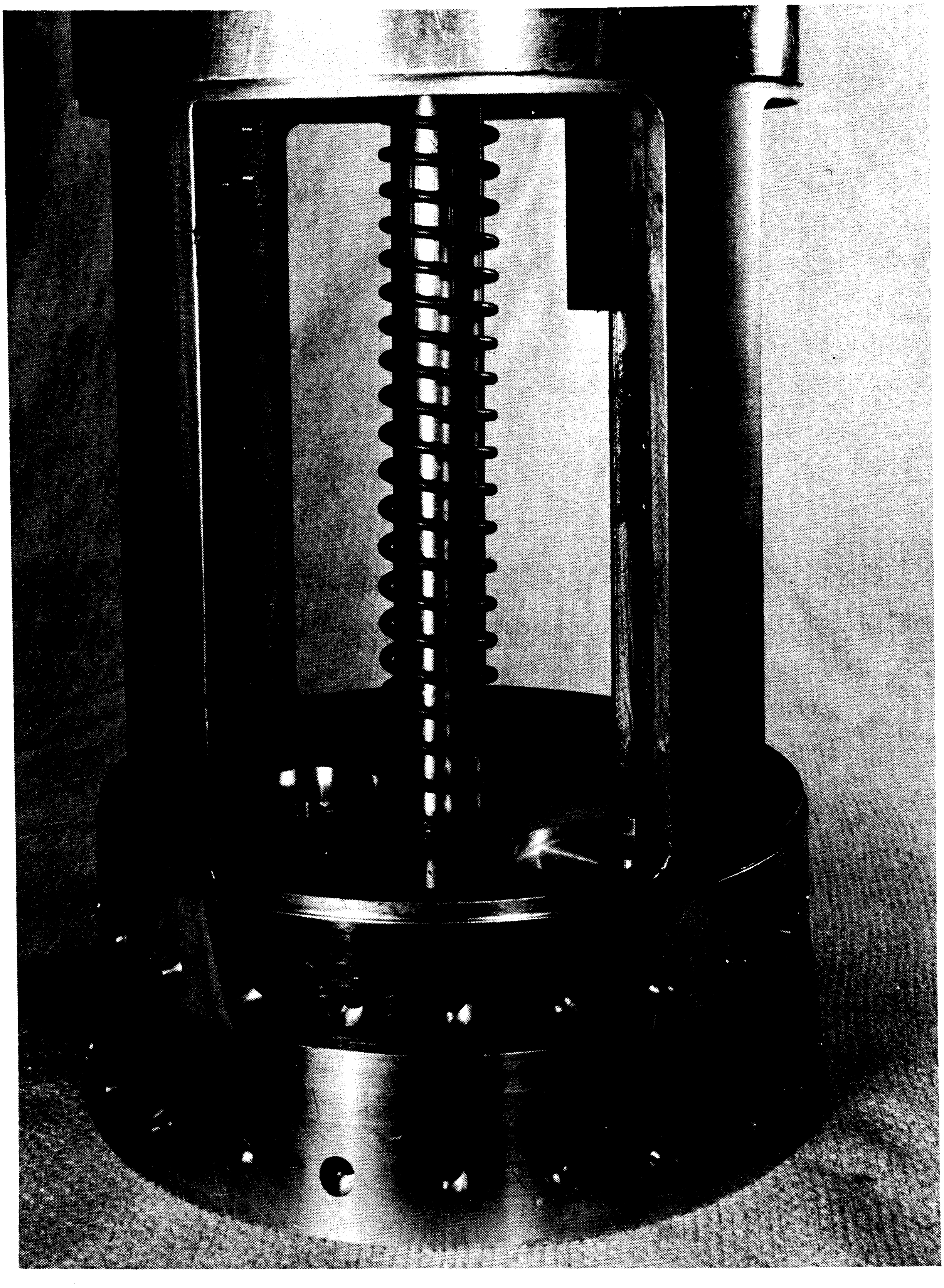

Fig. 44. Bottom section of nose cone with skin removed.

available in this compartment for a radar beacon when one is desired.

Figure 45 shows the assembled nose cone in flight-ready position. The radar beacon antenna can be seen mounted in the lower nose cone cover.

3.3.3. Electrical System.—The electrical system of the nose cone has two functions, namely, the pre-launch control of the 8-inch sphere instrument, and the ejection release circuitry.

Evaluation of sphere performance when it is installed in the nose cone just before flight depends on complete electrical isolation of the sphere from the rocket. To effect this, the top of the plunger on which the sphere rests is made of linen-base phenolic, and insulation material is attached around the inside of the nose cone where the sphere bears against the walls. Four adjustable, contoured feet are mounted on the nose cone walls to hold the sphere firmly against the plunger until ejection. These are also made from the linen-base phenolic material. Two round nylon screw heads, projecting from the plunger face, fit into holes in the perforated sphere and keep it from rotating on the plunger without any danger of retarding the sphere as it is ejected. These parts may be seen in Fig. 46.

The connection to the pull-off control pin at the base of the sphere is in the center of the plunger. Wires from this connection pass down through the plunger shaft, beneath the base plate and back up to the nose cone umbilical plug. These wires not only bring control Ledex operation and range indication to the block house, but bring sufficient rf from the sphere telemetry system outside the nose cone to enable a system check to be made before the rocket is launched.

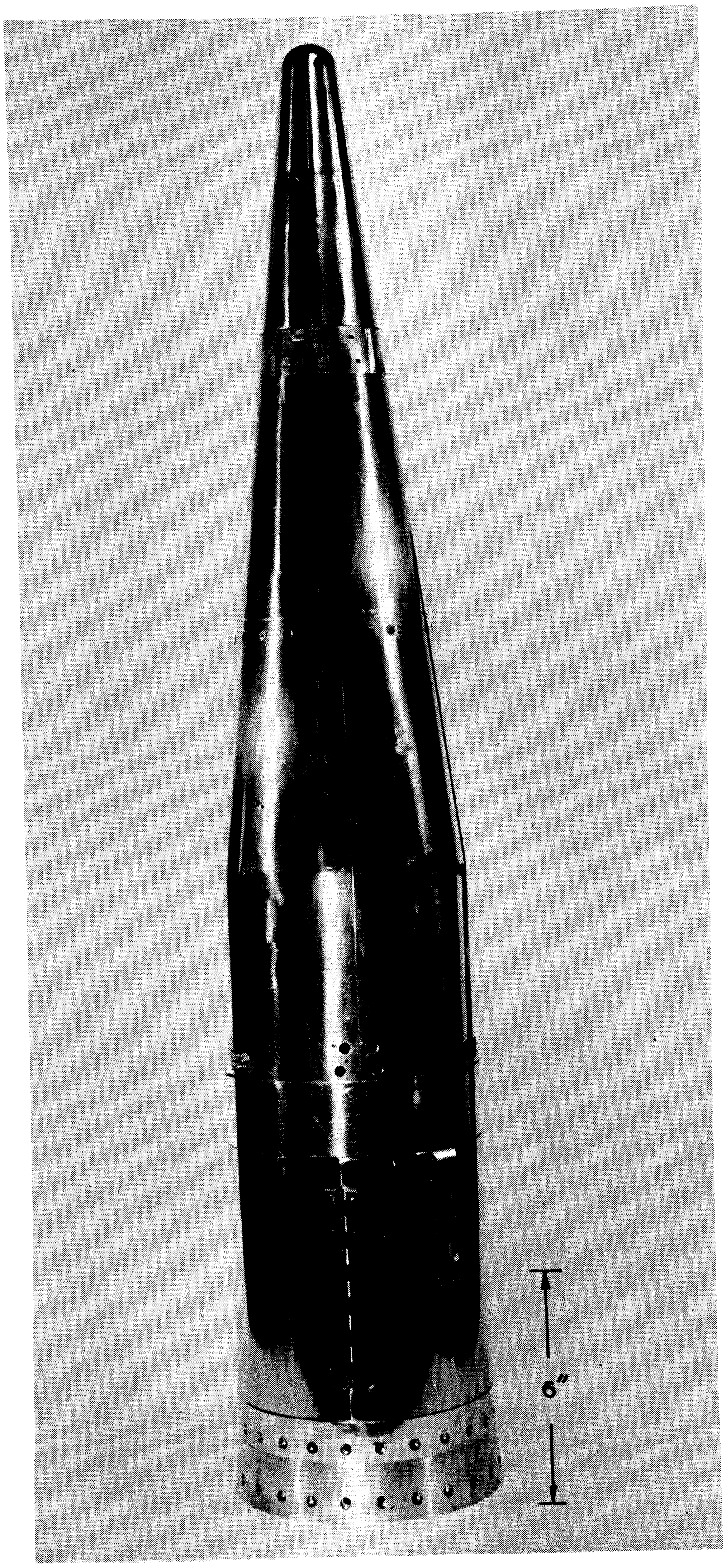

Fig. 45. Assembled nose cone.

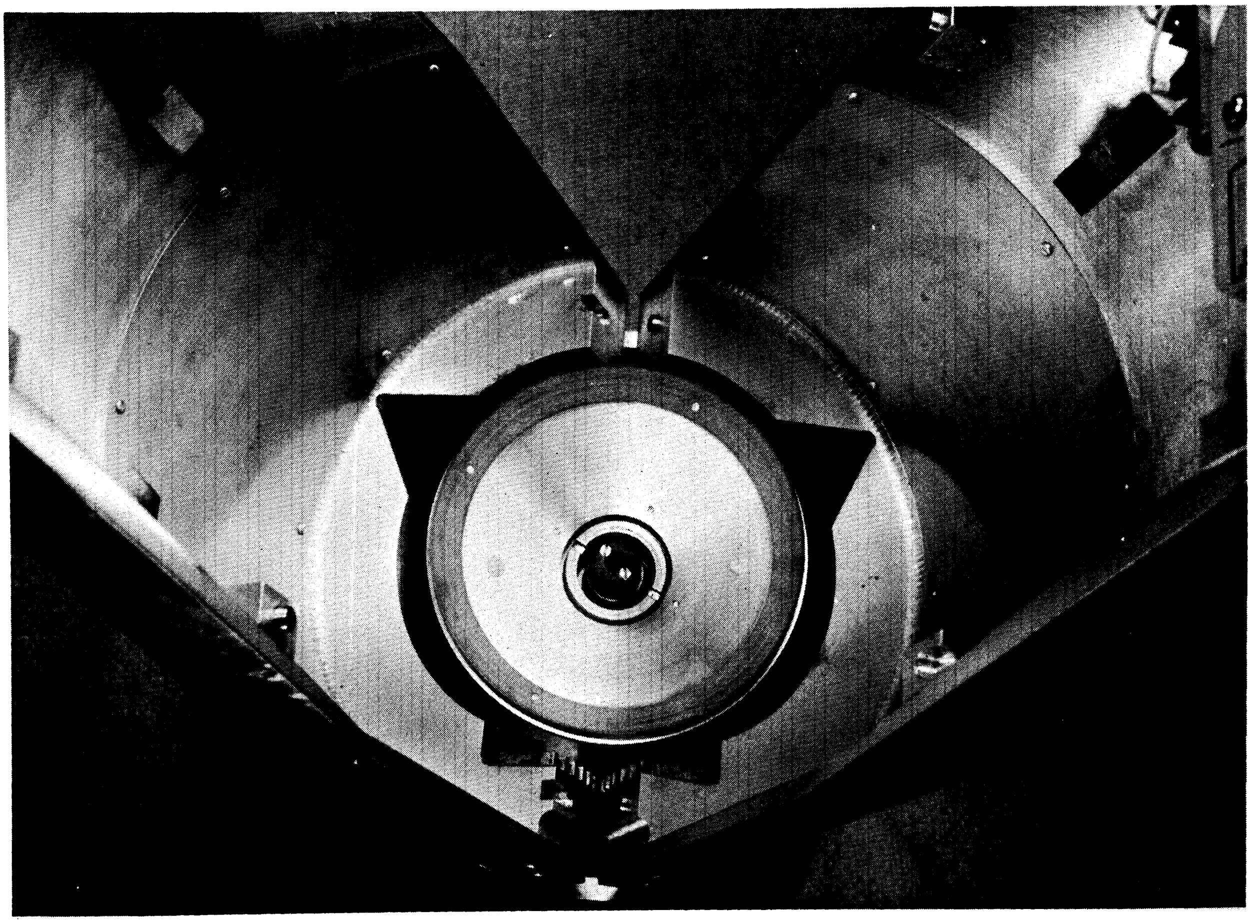

Fig. 46. Open nose cone showing plunger.

The second function of the nose cone's electrical system serves to apply detonation current to the squibs to initiate opening and ejection at a pre-selected time after launch. The system is contained in the conical section of the nose and is entirely automatic. Its essential components are a 6-volt battery pack, a mechanical "g" actuated timer, the 4 squibs, and a two-pin plug and receptacle to connect the two squibs in the other half of the split nose cone to the firing circuit.

The mechanical timer, which is started at launch by the rocket acceleration, is pre-set to close a microswitch approximately 60 sec after lift-off (depending on the vehicle) which connects the batteries to the four parallel-connected squibs. Both sides of the firing line are above rocket ground to permit normal operation if either side should become shorted to ground prior to ejection. The squib circuit is, however, returned to ground through a 10,000 ohm resistor to eliminate possible hazard from a static charge build-up.

Several other safety features are incorporated. A "rest" position is provided for one battery lead which disconnects the battery from the circuit until the lead is moved to the normal position prior to launch. The timer maintains a continuous short across the squibs until detonation, and two external plugs, one on each cone half, provide an additional short circuit until removed just prior to launch. Figure 47 is a circuit diagram of the nose cone wiring.

3.4. TESTING

The sphere and nose cone are subjected to a number of tests to insure, as nearly as possible with the facilities at hand, that satisfactory performance will be achieved during the actual flight.

The first test, usually, is a pressurization test of the sphere. It is desired that the gas within the sphere should not escape during flight to contaminate the environment; thus, the sphere is assembled, pressurized to 30 psi, and submerged in water for approximately 10 minutes to expose any leaks.

Before the instrumentation is assembled within the sphere, each circuit is tested, while in operation, over a temperature range from 0°F to 120°F to discover any excessive frequency or amplitude drift in output waveforms,

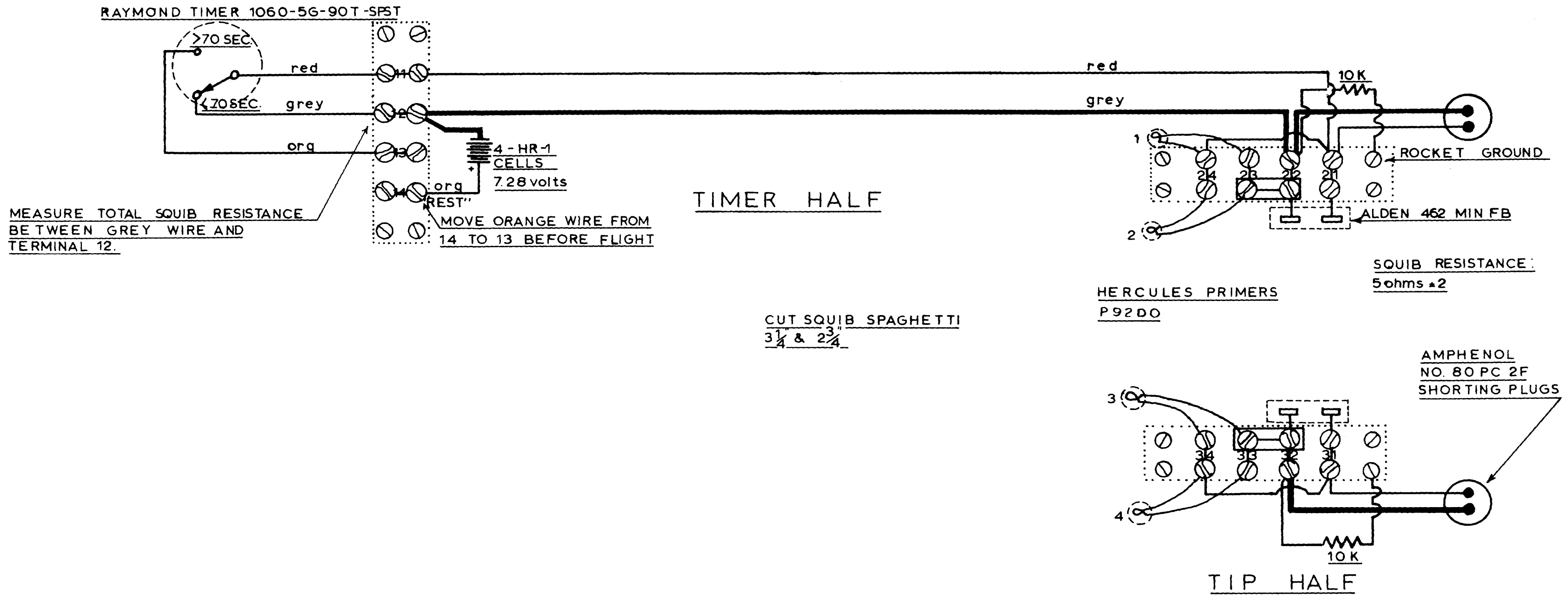

Fig. 47. Nose cone wiring diagram.

non-linearities, or component failures. Then the sphere is assembled, wired, and tested as a system, using external resistances to simulate the ionosphere. Oscillograph recordings are made of the output as received through the telemetry link. These are evaluated, and any interference problems in the system are solved.

When the sphere is completed and ready for flight, it is subjected to a 100g shock along the vertical axis and a 5 sec, lateral shake of 20g at 60 cps. During the test, the telemetry is monitored for any irregularities that may occur. Following this test, the sphere is taken into the field where rf signal intensity measurements are made and compared with predicted intensities to insure that the transmitter and antenna are performing normally.

Finally, a horizontal ejection test is conducted. This test is valuable in the evaluation of the ejection system, as well as giving the project personnel a rehearsal of the procedures that are to be followed at the launching site. In this test the sphere is suspended on a long harness and installed in the horizontal nose cone, the ejection system is cocked, and the squibs are armed. A count down is given, during which the sphere is turned on, the telemetry is monitored through the ground station, and the timer is actuated; simulating lift-off. All personnel are cleared from the area except for one strategically placed person who observes the ejection and secures the sphere before it can swing back towards the opened nose cone.

It can be seen that, by launch time, a large file of test data are available for aid in evaluating the flight behavior.

4.0. CONCLUSION

In the previous sections we have reviewed the history, theory, and implementation of the 8-inch sphere experiment. In the opinion of the authors the technique represents a valuable tool for the investigation of the ionosphere by direct measurements on relatively small sounding rockets. The instrument combines the advantages of the ion trap (particularly the measurement of ion temperature) with those of the classical Langmuir probe (the measurement of the electron temperature, and electron and ion density, in the undisturbed plasma outside the ion sheath which surrounds the instrument package). In particular, the technique is well suited to the study of the energy exchange mechanisms in the ionosphere by permitting simultaneous measurement of the ion and electron temperatures and their altitude dependance.

It should be noted that thermal equilibrium ($T_e = T_p = T_g$) can be expected to exist in the night time ionosphere and may exist in some regions in the daytime.[11] The use of the 8-inch sphere in such an environment will provide an excellent opportunity for checking the self consistency of the experimental methods by which T_e and T_p are derived and, if consistency is shown, permits a relatively simple direct measurement of gas temperature in these regions. Since ion and gas temperatures should be equal in both the daytime and night time ionosphere, the technique may prove useful to atmospheric research on a broader scale. For example, the gas temperatures derived from satellite drag studies[12] can be checked by direct measurement.

The above are some of the objectives of the authors in the coming series of two launchings now scheduled for the summer of 1962. One will be a night time measurement to evaluate the measurement technique, particularly regarding the ion trap operation, while the other will be launched at midday to determine the degree of thermal equilibrium as a function of altitude in the day time ionosphere.

5.0. ACKNOWLEDGMENTS

The authors are grateful to the following individuals who have contributed considerably to the development of the 8-inch sphere technique: to N. W. Spencer* for suggesting and directing the early development of the 8-inch ion trap-Langmuir probe; to George Carignan for supervision of and participation in the development, testing, and launching of the instruments; Walter Hoegy for verifying the theoretical development and for his helpful suggestions; Lyle Slider and Plymouth Freed for their assembly and testing of the instruments; Bud Campbell for his work in the mechanical design of the probe; and Rosann Burke for typing and editing the manuscript.

---

*Now with Goddard Space Flight Center, the National Aeronautics and Space Administration.

6.0. REFERENCES

1. Hok, G., Spencer, N. W., and Dow, W. G., "Dynamic Probe Measurements in the Ionosphere," *J. Geo. Res.*, *58*, No. 2 (1953).

2. Hok, G., Spencer, N. W., Dow, W. G., and Reifman, A., *Dynamic Probe Measurements in the Ionosphere*, Univ. of Mich. ERI Report, Ann Arbor, August, 1951.

3. Reifman, A., and Dow, W. G., "Theory and Application of the Variable Voltage Probe for Exploration of the Ionosphere," *Phys. Rev.*, *75*, 1311 A (1949).

4. Boggess, R. L., Brace, L. H., and Spencer, N. W., "Langmuir Probe Measurements in the Ionosphere," *J. Geo. Res.*, *64*, 1627 (1959).

5. Carignan, G. R., and Brace, L. H., *The Dumbbell Electrostatic Ionosphere Probe: Engineering Aspects*, Univ. of Mich. ORA Report 03599-6-S, Ann Arbor.

6. Spencer, N. W., Brace, L. H., and Carignan, G. R., "Electron Temperature Evidence for Non-Thermal Equilibrium in the Ionosphere," *J. Geo. Res.*, *67* (Jan. 1962).

7. Mott-Smith, H. M., and Langmuir, I., "The Theory of Collectors in Gaseous Discharges," *Phy. Rev.*, *28*, 727 (1926).

8. Krassovsky, V. I., "Soviet Exploration of the Ionosphere with the Help of Rockets and Earth Satellites," annals of the IGY, Vol. 12, Part 2, Pages 529-546, Pergamon Press, London, 1960.

9. Kanal, M., *Theory of Current Collection of Moving Spherical Probes*, Univ. of Mich. ORA Report 03599-9-S, No. JS-5, April 1962.

10. Brace, L. H., "Transistorized Circuits for Use in Space-Research Instrumentation," Univ. of Mich. Res. Inst. Report, Oct. 1959.

11. Serbu, G. P., Bourdeau, R. E., and Donley, J. L., "Electron Temperature Measurements on the Explorer VIII Satellite," *J. Geo. Res.*, *66*, 4313-4315, 1961.

12. Kallmann-Bijl, H. K., Daytime and nighttime atmospheric properties derived from rocket and satellite observation," *J. Geo. Res.*, *66*, 787-796, 1961.